ELSEVIER

Journal of Marine Systems 771 (2001) xxx

JOURNAL OF MARINE SYSTEMS

www.elsevier.nl/locate/jmarsys

Evolving the subspace of the three-dimensional multiscale ocean variability: Massachusetts Bay ☆

P.F.J. Lermusiaux *

Harvard University, Division of Engineering and Applied Sciences, Pierce Hall GCA, 29 Oxford Street, Cambridge, MA 02138, USA

Received 20 December 1999; accepted 10 October 2000

Abstract

A data and dynamics driven approach to estimate, decompose, organize and analyze the evolving three-dimensional variability of ocean fields is outlined. Variability refers here to the statistics of the differences between ocean states and a reference state. In general, these statistics evolve in time and space. For a first endeavor, the variability subspace defined by the dominant eigendecomposition of a normalized form of the variability covariance is evolved. A multiscale methodology for its initialization and forecast is outlined. It combines data and primitive equation dynamics within a Monte-Carlo approach.

The methodology is applied to part of a multidisciplinary experiment that occurred in Massachusetts Bay in late summer and early fall of 1998. For a 4-day time period, the three-dimensional and multivariate properties of the variability standard deviations and dominant eigenvectors are studied. Two variability patterns are discussed in detail. One relates to a displacement of the Gulf of Maine coastal current offshore from Cape Ann, with the creation of adjacent mesoscale recirculation cells. The other relates to a Bay-wide coastal upwelling mode from Barnstable Harbor to Gloucester in response to strong southerly winds. Snapshots and tendencies of physical fields and trajectories of simulated Lagrangian drifters are employed to diagnose and illustrate the use of the dominant variability covariance. The variability subspace is shown to guide the dynamical analysis of the physical fields. For the stratified conditions, it is found that strong wind events can alter the structures of the buoyancy flow and that circulation features are more variable than previously described, on multiple scales. In several locations, the factors estimated to be important include some or all of the atmospheric and surface pressure forcings, and associated Ekman transports and downwelling/upwelling processes, the Coriolis force, the pressure force, inertia and mixing.

Keywords: Multiscale; Evolving eigendecomposition; Dynamical variability analysis; Coastal ocean; Drifters; Monte-Carlo; Data assimilation; Ensemble and time-averaging

1. Introduction

During the past few decades, important progress has been made toward accurate forecasts of three-dimensional atmospheric and oceanic fields. Such forecasts have been issued for a wide range of scales, processes and purposes: for example, scales from

☆ These results were presented at the 31th International Liege colloquium on ocean hydrodynamics, "Three-dimensional ocean circulation: Lagrangian measurements and diagnostic analyses, May 1999," within a talk entitled, "The evolving subspace of the three-dimensional ocean variability."

* Tel.: +1-617-495-0378; fax: +1-617-495-5192.
E-mail address: pierrel@pacific.harvard.edu (P.F.J. Lermusiaux).

0924-7963/01/$ - see front matter © 2001 Published by Elsevier Science B.V.
PII: S0924-7963(01)00025-2

nearshore surface wave heights to global climate fluctuations, processes from rainfall to fisheries catches, and purposes from scientific inquiries to real-time operations and management. However, forecasts of the evolution of the variability in the statistical sense are only beginning to be carried out, considering scales of days to decades for the atmosphere, and months to years for the ocean. With the advent of efficient and multidisciplinary ocean observing and prediction systems (Smith, 1993; Robinson and the LOOPS group, 1999), accurate estimates of the future ocean variability are becoming feasible at higher resolutions. An objective of the present study is to forecast, decompose, organize and analyze the variability of multiscale physical ocean fields. The variability forecasts studied were carried out during a real-time multidisciplinary experiment that occurred in Massachusetts Bay (Mass. Bay) in late summer and early fall of 1998.

Variability refers here to the statistics of the differences between ocean states and a reference state. It depends on the reference state, on the ocean scales and processes considered, and on how their evolution is considered. Variability can be the statistics of the differences between the evolving ocean state and a state of reference either varying or constant, e.g. the average state over a certain period. It can be the statistics of the differences between possible ocean evolutions, i.e. evolutions of distinct but possible initial conditions and forcings, and a reference expected evolution. These are the two specific definitions considered here. The first one relates to time-averaging and usually deterministic evolutions, the second to ensemble-averaging and usually stochastic evolutions. Under certain circumstances, these two types of variability can be similar; this is briefly explored for Mass. Bay in Section 5, and a framework for comparisons is discussed in Appendix B. Another common type of variability corresponds to the statistics of the variations of simulated ocean fields in response to artificial changes in varied factors (e.g. add, remove or change the stratification, atmospheric effects). Variability is then associated with “what-if” scenarios or sensitivity studies. This latter definition is a common approach for seeking understanding, but it is not employed in the present experiment, which seeks to forecast and study the natural variability.

The Massachusetts Bay Sea Trial (MBST-98) was a pilot field experiment performed in a partnership including the programs of the Littoral Ocean Observing and Predicting System (Robinson and the LOOPS group, 1999), Advanced Fisheries Management and Information Service (Rothschild and the AFMIS group, 1999) and Autonomous Ocean Sampling Network (AOSN, Curtin et al., 1993). The objectives included trials of platforms and sensors, system integrations and a demonstration of concept for real-time multifield estimation. A specific scientific focus was phytoplankton and zooplankton patchiness. Simultaneous physical and biological data sets were obtained, characterizing structures and variabilities from tens of meters to tens of kilometers. These data were assimilated into interdisciplinary models, using optimal interpolation and error subspace statistical estimation (Lermusiaux, 1997, 1999a,b). Forecasts of the fields, and of error and variability covariances, were provided. These forecasts were used for adaptive sampling with three research vessels and two fleets of Autonomous Underwater Vehicles. Several hypotheses concerning the dynamical interactions among the circulation, productivity and ecosystem systems were inferred, as summarized in Robinson and the LOOPS group (1999) and Rothschild and the AFMIS group (1999).

Instead of the fields themselves, the focus here is on the dominant four-dimensional variability, hence the dominant changes and events. The variability forecast is obtained by a multiscale methodology combining the available data and numerical dynamical model within a Monte-Carlo approach. It is decomposed and organized via a singular value decomposition (SVD). The purpose is not to verify field forecasts (e.g. see Rothschild and the AFMIS group, 1999, for that), nor to analyze errors or the assimilation scheme (e.g. see Lermusiaux, 1999a,b), but to illustrate, classify and try to understand the dominant dynamical variability estimated. One may wonder why it is useful to forecast and decompose the variability. There are several reasons, e.g. (i) knowing the future dominant changes is often valuable, either for scientific understanding, management or monitoring; (ii) a dominant variability pattern is more significant statistically than a time-difference field; and (iii) these dominant three-dimensional and multivariate patterns can guide the dynamical analysis. In the case of MBST-98, several physical features and processes of the Bay are in fact located and studied based on the variability forecasts. Snapshots and tendencies of physical fields, and the trajectories of simulated Lagrangian drifters, are utilized to illustrate and confirm the dynamical value of the variability patterns.

The text is organized as follows. The dynamics of the Bay is briefly overviewed in Section 1.1. The main issues and approach are summarized in Section 2, the adaptive data sampling and dynamical model are in Section 3. The methodology to initialize, forecast and organize the variability is described in Section 4; the mathematical formulation is in Appendix A. The variability forecasts are exemplified, analyzed and evaluated in Section 5. The conclusions are in Section 6. In Section 4 and Appendix B, relationships with classic empirical orthogonal function (EOF) approaches are discussed. The timings of the forecasts exemplified are in Appendix C.

1.1. Aspects of the dynamics of Mass. Bay and scales of variability considered

The term Mass. Bay refers here to the semi-enclosed embayment adjacent to the Gulf of Maine (Fig. 1). Its dimensions are approximately 100×50 km. It is bounded to the north by Cape Ann, to the south by Cape Cod and partially to the east by Stellwagen Bank, which rises up to 30 m. The North and South Passages are two gateways to the Gulf. The deepest portion, about 80–90 m, is known as Stellwagen Basin. The average depth is about 35 m (Signell et al., 1993).

The mean circulation is observed to be cyclonic around the Bay, from north to south (Geyer et al., 1992). This mean flow from Cape Ann to Race Point is mostly driven by remote forcings from the Gulf of Maine coastal current and mean wind stress (Blumberg et al., 1993; Wallace and Braasch, 1996; Bogden et al., 1996; Brown, 1998). Based on an analysis of the previous literature and on several Observing System Simulation Experiments (e.g. Houtekamer and Derome, 1995; Atlas, 1997; Hackert et al., 1998) carried out at Harvard prior to MBST-98, an estimate of the main horizontal circulation features at the top of the pycnocline was compiled for stratified conditions (Fig. 1). We found that the Gulf of Maine coastal current can have three branches: one is the Mass. Bay coastal current, one enters the Bay but not Cape Cod Bay, and one flows along Stellwagen Bank, without entering Mass. Bay. Two gyres are often present, one in Cape Cod Bay and another to the north of Stellwagen Basin, but their sense of rotation is variable. Below the main pycnocline, we found that currents are usually of smaller amplitudes than, and of directions opposite to, the main buoyancy flow (i.e. thermal wind-driven flow). These bottom currents are influenced by surface wind and pressure forcings, bottom friction, geostrophic balance and the basin geometry. The four-dimensional results of MBST-98 confirm and refine these findings (see Section 5 for quantitative estimates).

The variability in Mass. Bay occurs on multiple scales, in response to internal dynamics and external forcings. The interannual variability has not been studied extensively, but the seasonal variability is known to be important (Geyer et al., 1992). For example, on yearly average, the wind stress in October to March is greater than in the rest of the year, especially than in summer (Geyer et al., 1992). During the stratified seasons, the mesoscale variability has been estimated to be significant (Signell et al., 1993), which is a result confirmed here (see Sections 5 and 6). At weather time scales, important wind-driven responses have also been observed (Geyer et al., 1992). The wind forcing often changes direction, with correlation times of the order of a day. Another time-scale emerging from MBST-98 corresponds to that of the storms capable of driving major changes in the buoyancy circulation (Fig. 1). During Aug. 17–Oct. 5, 1998, seven of such storms were found to occur, which is about one every week. These scales of a day to a week have not yet been analyzed comprehensively in Mass. Bay, with advanced data assimilation and numerical modeling. Most of the new findings of MBST-98 (Robinson and the LOOPS group, 1999; Rothschild and the AFMIS group, 1999) in fact relate to this time window. In Sections 5 and 6, it is mainly the combined influence of atmospheric weather forcings, internal pressure gradients and Coriolis force on the sub-mesoscale to Bay-scale variability (upwelling, downwelling, Bay-wide responses, frontogenesis, eddies, vortices, etc) which is considered.

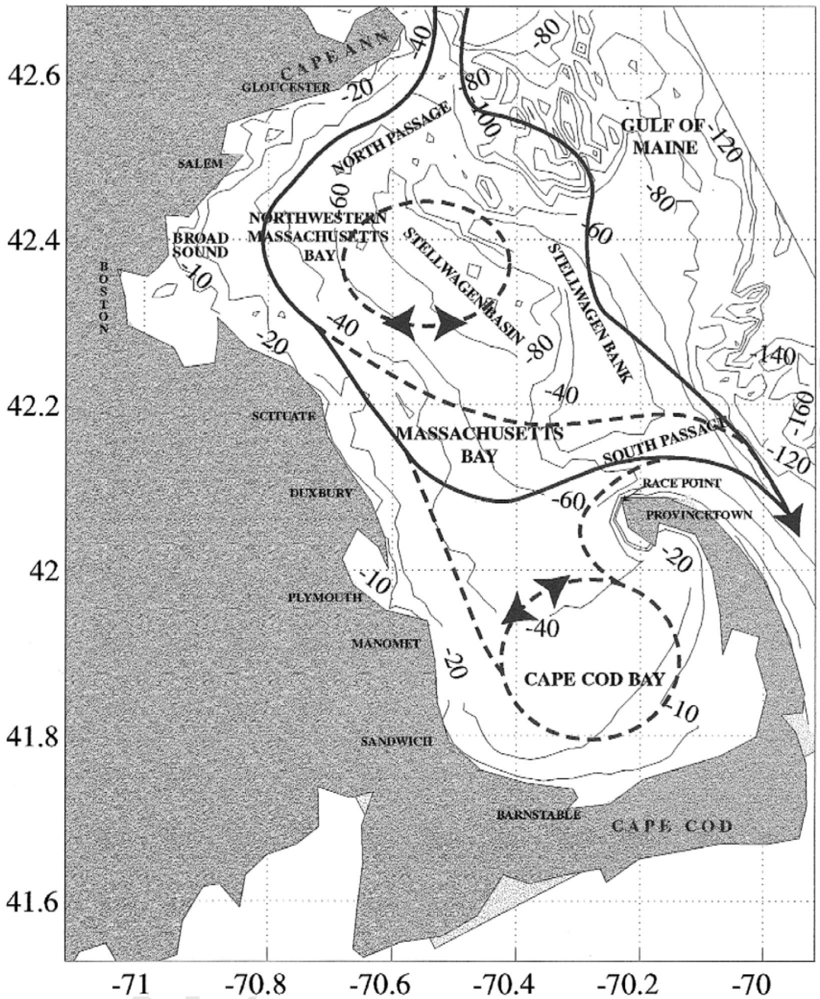

Fig. 1. Cartoon of horizontal circulation patterns for stratified conditions in Massachusetts Bay, overlying topography in meters (thin lines). The patterns drawn correspond to main currents in the upper layers of the pycnocline where the buoyancy driven component of the horizontal flow is often the largest. These patterns are not present at all times. The most common patterns are in solid lines, the less common are dashed. The cartoon combines interpretations of results described by Geyer et al., (1992), and references therein, with the numerical circulations of Observing System Simulation Experiments carried out starting a year and a half prior to MBST-98 (P.J. Haley and P.F.J. Lermusiaux, personal communication). These experiments used the Harvard Ocean Prediction System and assimilated historical in situ data provided by Prof. G.B. Gardner (personal communication). The cartoon agrees with, but does not contain all of the results of, the real-time component of MBST-98.

At higher frequencies and smaller scales, inertial oscillations, tidal effects and internal waves are important at certain times and locations. The generation and southwestward propagation of semidiurnal internal oscillations, bores and solitons above the western slope of Stellwagen Bank have been studied from observational (Halpern, 1971; Haury et al., 1979; Chereskin, 1983; Trask and Briscoe, 1983), experimental (Matsuura and Hibiya, 1990) and numerical–theoretical (Lee and Beardsley, 1974; Hibiya, 1988; Gerkema, 1996; Grimshaw et al., 1998) stand points. These processes, of largest amplitudes at the outer boundary of the Bay, are not studied here. Because of the bathymetry (Fig. 1), the strongest tidal currents are found near Race Point; some enhancement also occurs near Boston Harbor and Stellwagen Bank (Geyer et al., 1992; Signell and Butman, 1992). Although tides can lead to localized water exchanges near Race Point and Boston Harbor, tidal currents have not been observed to be an important transport mechanism in the Bay (Geyer et al., 1992). Mixing due to tidal effects and internal waves can however be important near Stellwagen Bank and in coastal areas (Geyer and Ledwell, 1997). Internal tidal currents increase turbulence levels in the bottom and coastal boundary layers, while internal waves are a source of shear in the thermocline.

Other dynamical processes that have been studied in Mass. Bay, many of which have been motivated by a sewage abatement project, include bottom friction and coastal boundary mixing (Signell and List, 1997; Geyer and Ledwell, 1997), zooplankton variability (Turner, 1992), biochemical and physical interactions (Kelly, 1997, 1998; Kelly and Doering, 1997, 1999), sewage pollutions (Tucker et al., 1999) and toxic blooms (Anderson, 1997).

2. Issues and approach

The ocean evolves in time and space via internal dynamical phenomena and in response to external body and boundary forcings. Events and resonant interactions occur over multiple scales, often intermittently and with strong similarities between occurrences. Most variations of oceanic properties are thus interconnected, structured and scale-dependent. As a result, by definition (Section 1), the oceanic variability can be expected to possess these intrinsic attributes (dynamic, eventful, structured, etc.)

Based on the above observations, regardless of their scope and spectral window (Nihoul and Djenidi, 1998), most comprehensive oceanic models involve multiple and coupled dynamical state variables. Similarly, a diverse, efficient and compatible mix of measurements has become the requirement for most four-dimensional and multidisciplinary investigations. Aiming for realistic field estimates, data assimilation (Daley, 1991; Ghil and Malanotte-Rizzoli, 1991; Bennett, 1992; Evensen, 1994; Wunsch, 1996; Robinson et al., 1998) is utilized to combine both models and data.

Trying to be as realistic as field estimates, the ocean variability is here also computed by combining dynamical models with data. Such an estimation of the variability is challenging, mainly for four reasons. Determining the ideal type and number of quantities that efficiently describe the ocean statistics is still an area of active research (e.g. Salmon, 1998, Chapters 5 and 6). The discrete dynamical models available are large, imperfect and complex. The ocean data are limited and noisy. Finally, ocean state evolutions, hence the variability, are often sensitive to initial conditions.

Addressing these four challenges one at a time, in the present endeavor, the variability is limited to its covariances or second-moments. This starting point is partly motivated by the fact that within all moments, the second one is often an important and useful characteristic of the variability in natural systems. Secondly, since realistic dynamical models are complex and large, an efficient representation of the covariances is necessary: their likely complex properties (three-dimensional, multivariate, multiscale, etc.) are here not removed, but their significant components or subspace are sought. Significance is presently measured based on a percentage of variance explained. The variability subspace is then defined by the “dominant” eigenfunctions of the variability covariance (Section 4). Its dynamics is presently forecasted via a Monte-Carlo approach (Section 4.2), mainly because of the likely efficacy of this method when nonlinearities occur. Thirdly, since the relevant data are usually limited, it is essential to use them all and often necessary to compensate their weaknesses by fitting their values to analytical models (Section 5.1). Fourthly, to limit the sensitivity to initial conditions, the dominant variability is initialized (Section 4.1) based on the complete dynamics and relevant data (Section 3).

3. Data and dynamical model

3.1. Data

During MBST-98, from Aug. 17 to Oct. 5, the hydrographic shipboard data added up to 215 conductivity–temperature–depth (CTD) profiles and the Autonomous Underwater Vehicle missions to an equivalent of 280 CTD profiles. These observations were gathered in three phases (Rothschild and the AFMIS group, 1999): the initialization surveys (Aug. 17–21), update surveys (Sep. 2–4) and 2 weeks of intensive engineering and scientific operations (Sep. 17–Oct. 5). To collect these hydrographic data, an adaptive sampling methodology was carried out in real-time. The sampling strategies were designed based on (i) ocean field forecasts assimilating the prior data, and (ii) forecasts of dominant error or variability covariances (variance and dominant eigenvectors, see Sections 5.2.2 and 5.2.3). The goals were to (i) sample the regions of most active or interesting dynamics, and (ii) minimize forecast uncertainties. Optimal strategies were also subject to weather and operational (platforms, sensors, schedules) constraints. Examples of the resulting real-time sampling patterns are shown in Fig. 2, illustrating the multiplicity of scales and variables measured.[1]

All CTD profiles used here were collected before and on Sep. 27. The other data employed consist of the: Fleet Numerical Meteorologic and Oceanographic Center (FNMOC) data for the computation of the atmospheric forcings; climatological data (LOC, Lozier et al., 1996) to estimate the Bay-scales of the initial fields in the outer Cape region only (Section 5.1.1); and satellite data for model calibrations.

3.2. Dynamical model

The numerical dynamical model used (Appendix A, Eq. (A1a)) is the nonlinear, stochastic primitive equation (PE) model of the Harvard Ocean Prediction System (HOPS; e.g. Robinson, 1996; Lozano et al., 1996; Lermusiaux, 1997). The state variables are the dynamical tracers, temperature T and salinity S, the barotropic transport stream function ψ, and the zonal (x) and meridional (y) internal velocities, $\hat{u}$ and $\hat{v}$, respectively; the corresponding fields/variability are henceforth called the PE fields/variability. The vertical coordinate system is a topography-following system ("double-sigma," e.g. Lozano et al., 1994). The tuning and calibration of the PE model started a year prior to MBST-98. During the real-time experiment, the values of the numerical and physical parameters were evolved in time, in accord with the incoming in situ, satellite and atmospheric data (see Rothschild and the AFMIS group, 1999, Appendix VI). The values of the main parameters listed in Table 1 were used during the last days of September and first week of October (early fall), which is the period considered in Section 5.

To analyze our results, several parametrizations are important,[2] e.g. that of the diverse mixing processes (Section 1.1). The horizontal subgrid-scale mixing and numerical noise filtering is carried out by applying a Shapiro filter (Shapiro, 1970) on the variations of the total velocity, tracers and barotropic vorticity tendency (see triplets F_u, F_v, F_T, F_S, $F_{\overline{\varpi}_t}$ in Table 1). The vertical mixing is a Laplacian mixing. The profiles of the vertical eddy coefficients are computed as a function of space, time and local physical fields (L.A. Anderson and C.J. Lozano, personal communication). Near the surface, a mixing-layer model transfers and dissipates the atmospheric forcings (wind-stress and buoyancy flux computed from daily 12GMT FNMOC data, and interpolated linearly in time). It first evaluates the local depth of turbulent wind-mixing or "Ekman depth" $h^e(x, y, t)$. This depth is assumed proportional to the "depth of frictional influence" that is limited by rotation, i.e. $h^e = E_k u^* / f_0$ (Rossby and Montgomery, 1935; Cushman-Roisin, 1994). In this similarity height relationship, the turbulent friction velocity $u^*(x, y) \doteq \sqrt{\|\tau\|/\rho_0}$ is computed from the wind stress vector τ and reference density ρ_0. The coefficient E_k is an empirical factor (Table 1) and f_0 is the Coriolis parameter. The final h^e is further constrained by adjustable bounds $h^e_{\min} \leq h^e \leq = h^e_{\max}$. Once h^e is computed, the vertical eddy coefficients within h^e are set to the empirical values A^e_v and K^e_v (Table 1). This vertical mixing-layer model is one of

[1] Note that most of the turbulence scales are not resolved by the 1.668-km model grid (Section 3.2). A usage of the turbulence data (Fig. 2f) is in fact the calibration of the sub-grid scales mixing parameters (Table 1).

[2] Based on 2 months of empirical experience, the relative uncertainty of the values given in Table 1 is near $\pm 25\%$. The forecasts being short (a few days to a week), smaller relative changes in the parameter values usually led to insignificant changes in skill.

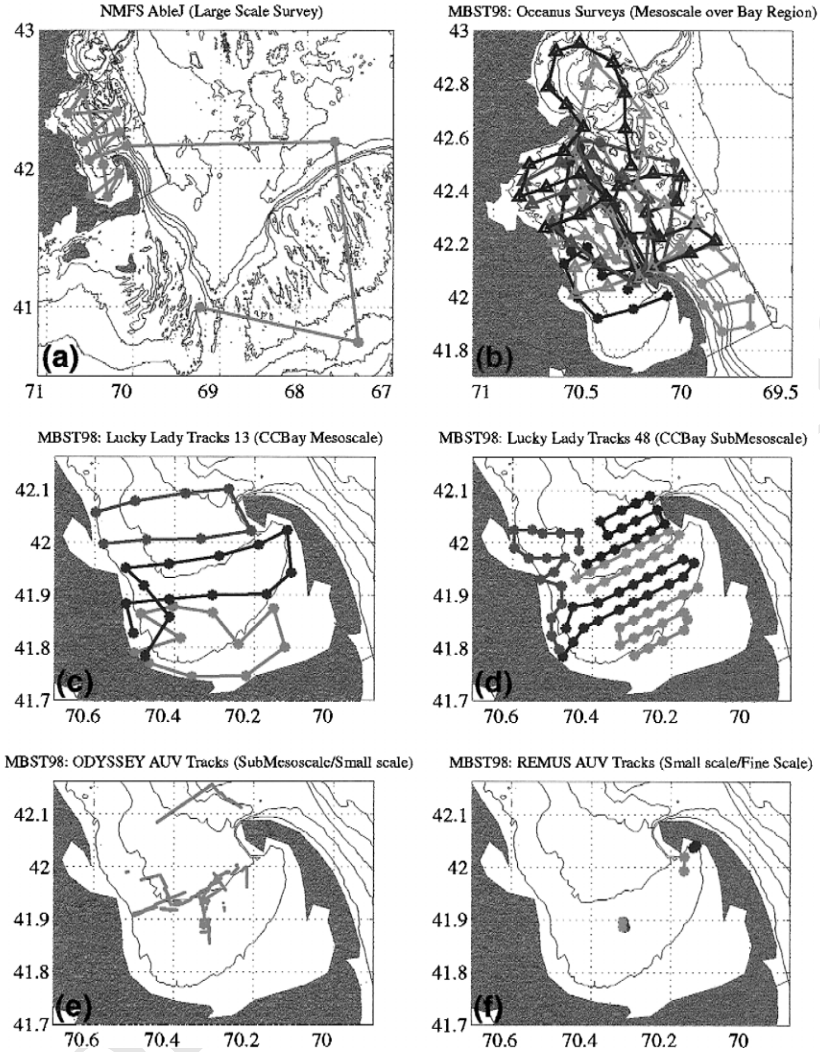

Fig. 2. Multiscale adaptive sampling patterns. (a) Bay scales and external oceanic forcings (note adapted zigzag in Gulf of Maine and over Georges Bank), with CTD, Plankton and Fluorescence sensors. (b) Mesoscales, mainly outside of Cape Cod Bay, and in the open boundary regions, with CTD sensors. (c) Mesoscale and (d) sub-mesoscales, mainly in Cape Cod Bay, with CTD and TAPS (Dr. D.V. Holliday, personal communication) sensors. (e) Sub-mesoscales, mainly in Cape Cod Bay, with CTD and Fluorescence sensors (Dr. J. Bellingham, personal communication). (f) Turbulent scales in Cape Cod Bay, with CTD and ADV-O sensors (Dr. Ed. Levine, personal communication). For the R/V Oceanus and Lucky Lady (two main platforms), sampling patterns were designed daily (a pattern requires about 9–12 h of ship-time). On (b)–(d), different colors distinguish such daily patterns and symbols (triangle, diamond, circle, etc.) indicate sampling positions.

the common results of more complex models (e.g. Mofjeld and Lavelle, 1984; Garwood et al., 1985; Stigebrandt, 1985; Large et al., 1994). Below h^e, eddy viscosities and diffusivities are estimated based on the local gradient Richardson number Ri, using a scheme similar to that of Pacanowski and Philander (1981). Where $Ri(x, y, z, t)$ is ≥ 0, the eddy viscosity and diffusivity are set to $A_v = A_v^b + (v_0)/(1+5Ri)^2$ and $K_v = K_v^b + (v_0)/(1+5Ri)^3$. In this shear vertical mixing scheme, the adjustable

Table 1
Dynamical model parameters

Numerical parameters	
Centroid latitude and longitude	42.31N, −70.48W
Domain extension	86.74 km (x), 148.45 km (y)
Grid resolution	1.668 km
Grid size	53 (x), 90 (y), 16 (levels, double sigma)
Time step	225 s
State vector size	310,050
Physical parameters	
Horizontal mixing/shapiro filter	F_u, F_v: 4−1−1; F_T, F_S: 4−1−1; $F_{\overline{\omega}_t}$: 2−2−1
Surface vertical mixing response to atmospheric forcing (Ekman layer)	$E_k = 0.040$; $h^e_{min} = 1$ m; $h^e_{max} = 9$ m; $A^e_v = 15$ cm^2 s^{-1}; $K^e_v = 0.75$ cm^2 s^{-1}
Interior shear vertical mixing	$A^b_v = 0.5$ cm^2 s^{-1}; $K^b_v = 0.01$ cm^2 s^{-1}; $\upsilon_0 = 50$ cm^2 s^{-1}; $A^{cvct}_v = 50$ cm^2 s^{-1}; $K^{cvct}_v = 50$ cm^2 s^{-1}
Open boundary conditions	$\hat{u}$,$\hat{v}$: ORI; T,S: ORI; ψ: ORE 1/2; $\overline{\omega}_t$: ORE 1/2
Drag coefficient	$C_d = 0.0025$
Rayleigh coastal friction	$\tau_c = 5400$ s; $L_c = 1.668$ km
Rayleigh bottom friction	$\tau_b = 10{,}800$ s; $H_b = 2$ bottom levels

parameters are the background coefficients, A^b_v and K^b_v, and shear eddy viscosity at $Ri = 0$, denoted by υ_0 (Table 1). For negative Ri's, the convective values A^{cvct}_v and K^{cvct}_v are utilized. These coefficients A^{cvct}_v and K^{cvct}_v are also used at all depths and locations where the water column is statically unstable. At the open boundaries, conditions based on an Orlanski radiation (ORI/ORE) scheme (Orlanski, 1976; Lermusiaux, 1997) are employed. Across coastlines, the normal flow and tracer flux are set to zero. Along coastlines, the tangential flow is weakened using a Rayleigh friction of relaxation time τ_c and Gaussian decay horizontal-scale L_c (Table 1). At the bottom, a dynamic stress balance is applied to the momentum equations, with a drag coefficient C_d. An additional Rayleigh friction of relaxation time τ_b and Gaussian decay vertical-scale H_b is employed to parametrize a simple bottom boundary layer for momentum.

To represent the mixing due to tidal effects and internal waves (Section 1.1), a mixing parametrization increasing in accord with tidal forcing fields was also utilized. However, this enhanced mixing did not lead to ocean fields significantly different from these produced from the model (Table 1) without it (P.J. Haley, personal communication). For the data available (Section 3.1) and resolution employed, the differences were within uncertainty estimates.

4. Methodology

Considering the dynamical equations for the ocean state in their discretized form in space, with the above approach, the goal is to initialize and evolve the "dominant" eigendecomposition of the (normalized[3]) variability covariance matrix, combining data and dynamics. This "dominant" eigendecomposition or variability subspace corresponds to the eigenvectors and eigenvalues which account for most of the (normalized) variability variance. A mathematical formulation of these statements is outlined in Appendix A. Except for a few shorthands, the conventions of Ide et al. (1997) are followed. In particular, an estimate of the dominant eigendecomposition of the variability covariance at time t is denoted by $\mathbf{B}^p(t) = \boldsymbol{E}(t\Pi(t)\boldsymbol{E}^{\mathrm{T}}(t)$, where the diagonal of $\Pi(t)$ contains the largest p eigenvalues and the columns

[3] Multivariate covariances are dimensional, but all decompositions are carried out on non-dimensionalized covariances so as to be unit-independent (see Appendix A). To lighten the text, the term "normalized" is however usually omitted.

of $\boldsymbol{E}(t)$, the corresponding eigenvectors. The definitions of other symbols employed are in Appendix A.

In a sense, combining data and dynamics to evolve the variability subspace connects the EOF representation of data (e.g. von Storch and Frankignoul, 1998) with the dynamical normal mode decomposition (e.g. Kundu, 1990). The classic version of these two decompositions is extended: all properties of the variability subspace, e.g. its size p, its eigenbase and its eigenvalues, are here allowed to vary with time, on multiple scales, as a function of field variations. In Appendix B, a few relations between the classic spatial EOFs, or the eigendecomposition of time-averaged sample variability covariances, and the present eigendecomposition of dynamically evolving variability covariances are discussed. The methodology utilized in Section 5 to initialize and forecast the variability subspace is outlined next.

4.1. Initialization of the variability subspace

Following Section 2, both data and dynamics are used to estimate $\mathbf{B}^p(t_0)$, where t_0 denotes the initial time. In situ data are here temperature and salinity profiles (Section 3.1), on multiple time and space scales. The dynamics is governed by a stochastic primitive equation model (Section 3.2 and Appendix A). The reference primitive equation state at t_0 is denoted by $\boldsymbol{\varepsilon}\{\boldsymbol{x}\}(t_0)$.

The above situation is typical for the initialization scheme of Lermusiaux et al. (2000). This scheme proceeds in two stages. Briefly, for the variables, regions and regimes with synoptic (recent) data, the dominant variability is specified, either directly from these data or via an analytical model fit to these data. This determines the “observed” portions of the variability subspace at t_0, accounting for the measured complexities of nature. In the second stage, the “non-observed” portions are built by cross-covariances, in accord with the observed ones, by carrying out an ensemble of adjustment dynamical model integrations. For each of such integrations, the initial state is first perturbed by a random combination of vectors lying in the “observed” portions of the variability subspace (result of the first stage). The equations of the model in Appendix A, Eq. (A1a), which govern the lesser sampled (non-observed) variables, are then integrated forward in time, until these variables are statistically adjusted to the dynamical model and observed variability. In doing so, all variables and parameters perturbed based on the observed variability are here kept fixed (reduces integration costs and avoids numerical errors). The statistical adjustment is usually reached when the time-rates-of-change of the non-observed variables stabilize within a range adequate for the dynamics of interest (the duration of integration varies with the dynamics and data at hand, and with the quality of the first-guess at the fields to be adjusted). Each integration leads to one dynamically adjusted state. Subtracting the reference $\boldsymbol{\varepsilon}\{\boldsymbol{x}\}(t_0)$ from these adjusted states leads to an ensemble of variability samples, which is normalized and organized by SVD. The ensemble size, or total number of adjustment integrations, is increased until it is estimated large enough to explain most of the variability variance. This is assessed by a convergence criterion which measures the added value of new samples to the covariance estimate. The criterion is here based on the SVD of the zero-mean, normalized variability samples (Lermusiaux, 1997; Lermusiaux and Robinson, 1999). When the criterion is satisfied, the estimate $\mathbf{B}^p(t_0) \doteq \boldsymbol{E}_0\, \boldsymbol{\Pi}_0\, \boldsymbol{E}_0^{\mathrm{T}}$ is available.

The above initialization scheme has roots in the relations discussed in Appendix B. Its first stage computes the observed portions of the variability using past samples, as a fading-memory time-averaged covariance $\mathbf{C}_\lambda(t_0)$ (see Appendix B.2). Its second stage completes $\mathbf{B}^p(t_0)$ by ensemble averaging, integrating the equations of Appendix A, Eqs. (A4a,b) that correspond to the non-observed variability. The specifics of the present procedure are in Section 5.1.2.

4.2. Forecast of the variability subspace

The forecast of $\mathbf{B}^p(t)$ is carried out via a sequential Monte-Carlo approach (e.g. Robert and Casella, 1999; Chen et al., 2000), simulating Appendix A, Eqs. (A4a)–(5) by carrying out an ensemble of perturbed forecasts. The perturbed initial states are created based on $\boldsymbol{\varepsilon}\{\boldsymbol{x}\}(t_0)$ and $\mathbf{B}^p(t_0)$. Using the model of Appendix A, Eq. (A1a), these states are evolved forward in parallel, up to the time t for which a forecast of $\mathbf{B}^p$ is desired. Variability samples from the ensemble mean, estimate of $\boldsymbol{\varepsilon}\{\boldsymbol{x}\}(t)$ in

Appendix A, Eq. (A2) are then computed, normalized, and their SVD evaluated. This is continued, i.e. new perturbed integrations of Appendix A, Eq. (A1a) carried out and the rank p of $\mathbf{B}^p$ increased, until the added value of new variability samples is found small enough or insignificant based on a convergence criterion. At that point, $\mathbf{B}^p(t)$ is obtained. The procedure can then be reproduced for the next forecast time.

For nonlinear systems, this scheme is a simple method for tracking the evolving subspace of the variability covariance. The nonlinear and stochastic terms continuously excite new directions in the state space and the size p of the subspace varies based on an convergence criterion (p increases/decreases so that the subspace explains most of the variability variance). For linear systems, more of such subspace trackers have been derived (e.g. Oja, 1992; Dehaene, 1995; Haykin, 1996; Lermusiaux, 1997).

5. Dominant variability covariance forecasts

The real-time simulation illustrated and studied in detail corresponds to the four days between Sep. 27–Oct. 1, 1998. The primitive equation fields and dominant variability covariance were first initialized for Sep. 27 (Section 5.1) and then forecasted (Section 5.2). Note that the first 2 model-days are hindcasts carried out to allow the initial fields and dominant variability to adapt to the complete, wind-forced dynamics (Appendix A, Eqs. (A1a) and (A4a,b) . The last 2 model-days (Sep. 29 to Oct. 1) are the actual forecasting period. The elapsed-times of these computations are given in Appendix C.

5.1. First-guess initial conditions for Sep. 27

5.1.1. Initial primitive equation fields

The gridded tracer fields for Sep. 27 were obtained by two-scale objective analysis (Robinson, 1996; Lozano et al., 1996) of the data available at that time, on 22 horizontal levels. The two scales were the Bay scales and mesoscales. For each level, the non-dimensional (0 to 1) historical and synoptic data error variances were calibrated to 0.3 and 0.15, respectively, based on experience and on improvements of skill by trial-and-error. The non-dimensional horizontal covariance function utilized was a "Mexican hat" (negated second-derivative of a two-dimensional Gaussian function). Bay scales were first mapped, using the 142 profiles collected from Sep. 17 to 27 and 10 LOC climatological profiles located east of Cape Cod so as to constrain the outflow of the Gulf of Maine coastal current. For these Bay scales, the zero-crossings were fit to data at 60 km and spatial decay-scales at 25 km. The mesoscale correction was then added to the Bay scales, based only on the profiles gathered during Sep. 17–27. The mesoscale zero-crossings were fit to data at 20 km, spatial decay-scales at 6.5 km and decorrelation-time at 5 days (time centered on Sep. 27). Once the tracer fields were gridded, a first-guess at the initial flow conditions was computed assuming thermal-wind balance, up and down from a level of no motion fit at 35 m. In that computation, the barotropic transport was constrained along the open boundary of the domain (Fig. 1) to account for the Gulf of Maine coastal current: an inflow of 0.08 Sv was imposed at the northern side, zero transport at the eastern side and an outflow of 0.08 Sv at the southern side (most corresponding barotropic velocities, function of depth and transport gradient, are between 0 and 10 cm/s, the maxima reach 20 cm/s). This choice was based on calibrations prior to Sep. 27 and in Geyer et al. (1992).

The resulting initial field estimate is illustrated in Fig. 3. The situation on Sep. 27 is interesting because it was preceded by a strong northerly (from the north) wind event on Sep. 23, and then a sustained period of weak to medium westerly–southwesterly winds from Sep. 25 to 27. As a result, upwellings have occurred along both the east and west coastlines of Cape Cod Bay and anticyclonic vortices have been formed on each side of the open-boundary of Cape Cod Bay. The vortex in Cape Cod Bay (Fig. 3) has a weak western side, in part because of the westerly component of the recent winds (Sep. 25–27), which feeds a transport to the south. The Gulf of Maine coastal current is estimated to be mainly outside of Mass. Bay, meandering around several vortices and topographic features (North Passage, Stellwagen Bank, South Passage). Its largest horizontal velocities (at 10 m, reaching 35 cm/s) are in a convergence zone southeast of Cape Ann. A weak

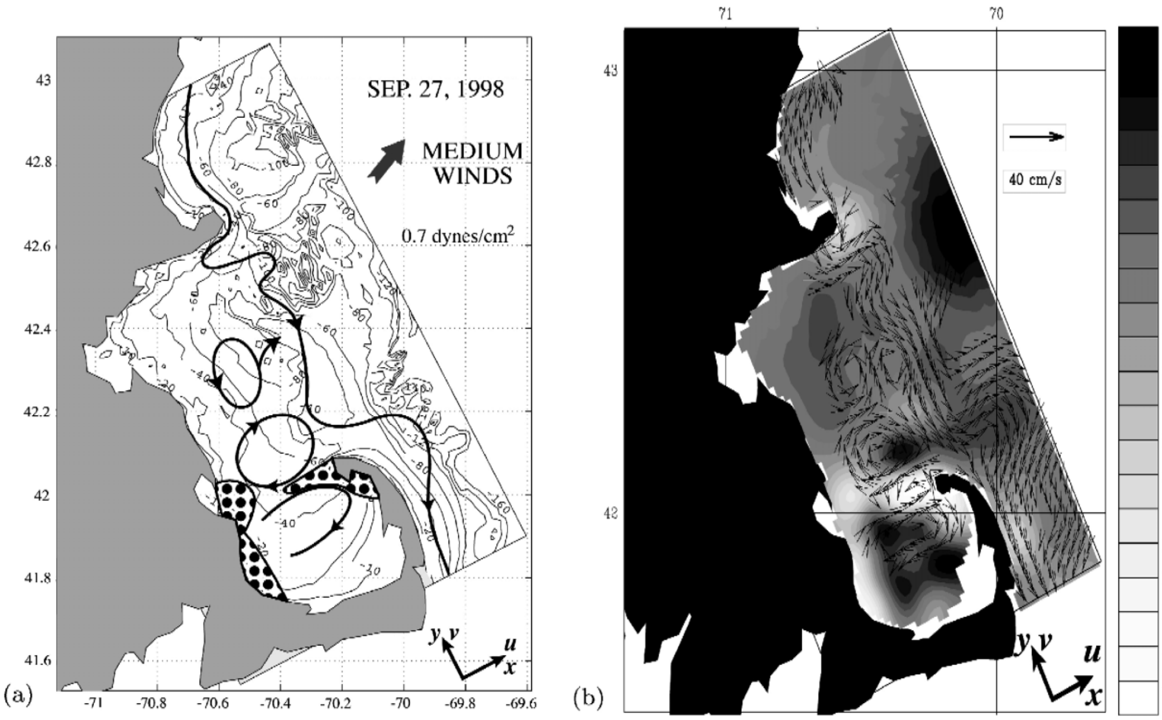

Fig. 3. First-guess initial field conditions for Sep. 27, 1998. (a) Circulation patterns for the main buoyancy currents below the surface Ekman mixing-layer, in the upper layers of the pycnocline, as on Fig. 1. These layers are near 10 m (in general, from about 5 to 25 m). Only the currents of magnitude larger than 5 cm s^{-1} are considered. The main direction and strength of the FNMOC winds at 12:00 GMT are indicated by the vane arrow and amplitude in dyn/cm^2, respectively (weak, blue arrow; medium, green arrow; strong, red arrow). The coastal upwelling (downwelling) regions, also for the upper layers of the pycnocline, are hachured in blue (red). The underlying topography is in meters. (b) For reference, temperature (°C) at 10 m, overlaid with horizontal vectors at 10 m (scale arrow is 0.4 m/s). The horizontal coordinate system used in the manuscript is also drawn (bottom-right corners): the "zonal" and "meridional" directions are rotated with the domain. Note that the panels correspond to different projections, hence the different distortions.

cyclonic vortex is present in northern Mass. Bay. Several sub-mesoscale eddies are in between the Gulf of Maine coastal current and mesoscale vortices, with branches and filaments, but their velocity estimates are usually smaller than 5 cm s^{-1}.

5.1.2. Initial variability subspace

In the first stage of the variability initialization (Section 4.1), the tracer components $\mathbf{B}^{p}_{\mathrm{trc}}(t_0)$ of $\mathbf{B}^{p}(t_0)$ were assumed "observed". The measurements utilized consist of the 142 CTD profiles collected from Sep. 17 to 27 (Section 3.1). The variations of the tracer fields with respect to their expected Sep. 27 state $\boldsymbol{\varepsilon}\{\boldsymbol{x}\}(t_0)$ (Section 5.1.1) are first expanded into vertical functions and truncated, leading to a Kronecker product expansion of the tracer covariance matrix,

$$\mathbf{B}_{\mathrm{trc}}(t_0) = \sum_{i,j=0}^{I,J} \mathbf{C}^{z}_{i,j} \otimes \mathbf{C}^{r*}_{i,j}. \tag{1}$$

In Eq. (1), the $\mathbf{C}^{z}_{i,j}$'s and $\mathbf{C}^{r*}_{i,j}$'s are, respectively, the weighted vertical and non-dimensional (*) horizontal, tracer covariance matrices associated with vertical modes i and j. It is further assumed that: (i) the expansion (1) is divisible into sequential contributions of three independent scales, the Bay scale, mesoscale and sub-mesoscale; and (ii) within each scale or contribution, the $\mathbf{C}_{i,j}^{r*}$'s are identical. Expansion (1) then becomes,

$$\mathbf{B}_{\mathrm{trc}}(t_0) = \sum_{w=1}^{3} \mathbf{B}_w = \sum_{w=1}^{3} \mathbf{C}_w^z \otimes \mathbf{C}_w^{r*}, \qquad (2)$$

where w is the index for the three spectral windows. Note that the above two assumptions are only approximations: they reduce the number of covariances to estimate and, thus, the data requirements of a more general scheme (Lermusiaux et al., 2000). The vertical covariances $\mathbf{C}_w^z$, $w=1, 2, 3$, are here directly specified, computing the vertical EOFs of recent ($t \leq t_0$, but synoptic) scale-filtered tracer data residuals. The horizontal covariances $\mathbf{C}_w^{r*}$ are evaluated from an analytical model fit to these residuals, so as to augment the limited horizontal correlation information present in the data (Fig. 2). The horizontal functions employed are the "Mexican hats" used in the field initialization (Section 5.1.1). Once evaluated, the $\mathbf{C}_w^{r*}$ are simply eigendecomposed. The significant rank-p_w eigendecomposition of each $\mathbf{C}_w^z \otimes \mathbf{C}_w^{r*}$, denoted here by $\mathbf{B}_w^{p_w} = \boldsymbol{E}_w \boldsymbol{\Pi}_w \boldsymbol{E}_w^{\mathrm{T}}$, is then obtained using Kronecker product properties (Graham, 1981). Eq. (2) is thus finally reduced to $\mathbf{B}_{\mathrm{trc}}^p(t_0) \cong \sum_{w=1}^3 \mathbf{B}_w^{p_w}$. Note that the sub-mesoscale component of $\mathbf{B}_{\mathrm{trc}}^p(t_0)$ was not initialized in real-time, mainly because, over the full domain, there were not enough sub-mesoscale data synoptic to Sep. 27 (Fig. 2). Hence, the sum in Eq. (2) was limited to the Bay-scale and mesoscale.

In the second stage (Section 4.1), the non-observed velocity components of $\mathbf{B}^p(t_0)$ are built by cross-covariances, in accord with $\mathbf{B}_{\mathrm{trc}}^p(t_0)$. Presently, the columns of each $\boldsymbol{E}_w$ were used one at a time to perturb the initial tracer fields, i.e. $\boldsymbol{x}_{\mathrm{trc}}^j(t_0) = \boldsymbol{x}_{\mathrm{trc}}(t_0) + \boldsymbol{E}_w \boldsymbol{\Pi}_w^{1/2} \sqrt{p_w}\, \boldsymbol{e}^j$, where the $\boldsymbol{e}^j$'s are base vectors of size p_w. To build the velocity fields in dynamical accord with $\boldsymbol{x}_{\mathrm{trc}}^j(t_0)$, the linear momentum equations were integrated forward in time, for 1 model-day, keeping $\boldsymbol{x}_{\mathrm{trc}}^j(t_0)$ fixed. As an example, the first two mesoscale variability samples that result from two of such adjustment integrations are shown in Fig. 4. In total, 300 integrations were carried out, mainly because of human time constraints (e.g. 1 day at sea). For that size, 76.8% of the mesoscale tracer variance was estimated to be explained. The complete $\mathbf{B}^p(t_0) = \boldsymbol{E}_0 \boldsymbol{\Pi}_0 \boldsymbol{E}_0^{\mathrm{T}}$ was ultimately obtained from the SVD of the normalized PE variability samples.

5.2. Forecasts for Oct. 1

To start the Monte-Carlo forecast of $\mathbf{B}^p$ for Oct. 1 (Section 4.2), the ensemble of perturbed initial conditions $\boldsymbol{x}^j(t_0)$ was created using $\boldsymbol{x}^j(t_0) = \mathbf{x}(t_0) + \boldsymbol{E}_0 \boldsymbol{\Pi}_0^{1/2} \boldsymbol{u}^j$, where the $\boldsymbol{u}^j$'s were realizations of the Gaussian random vector $\boldsymbol{u} \in R^{300 \times 1}$ of zero-mean and identity covariance. Each of these $\boldsymbol{x}^j(t_0)$ was then integrated for 4 days using Appendix A, Eq. (A1a), leading to the ensemble of forecasts $\boldsymbol{x}^j(t)$. As j increased, a similarity coefficient was repetitively evaluated, comparing current and previous estimates of the dominant variability covariance based on a variance measure (e.g. Lermusiaux, 1997, 1999a). The coefficient became close enough to 1 after 296 perturbations. Monte-Carlo integrations were then stopped. The forecast $\mathbf{B}^p(t) = \boldsymbol{E}_t \boldsymbol{\Pi}_t \boldsymbol{E}_t^{\mathrm{T}}$ was obtained from the SVD of the 296 normalized, zero-mean variability samples for Oct. 1. As discussed in Appendix B and shown in Sections 5.2.2 and 5.2.3, this $\mathbf{B}^p$ is related to the evolution of the fields themselves. The field forecast is thus described next (Section 5.2.1), prior to the variability standard deviation and eigenvector forecasts (Sections 5.2.2 and 5.2.3).

5.2.1. Primitive equation field forecasts

The 4-day evolution of the main horizontal currents in the top layers of the pycnocline is represented in Fig. 5. During this period, the wind and associated pressure forcings are important global controls of this buoyancy circulation, at times setting-up 3D Bay-wide responses or modes (see Sections 5.2.2 and 5.2.3), as has been observed also elsewhere (e.g. Candela and Lozano, 1995). The

Fig. 4. Construction of the initial physical variability subspace estimate for Sep. 27: adjustment momentum integrations for $w=2$ in Eq. (2). (a) Perturbation of the shape of the first dominant 3D mesoscale tracer eigenvector (1.2% of the 3D tracer variance) and its PE adjusted velocity response. (b) As (a), but for the second eigenvector (1.1% of the 3D tracer variance). All values are dimensional. For interpretations, recall that horizontal coordinates are "domain rotated" (see Fig. 3).

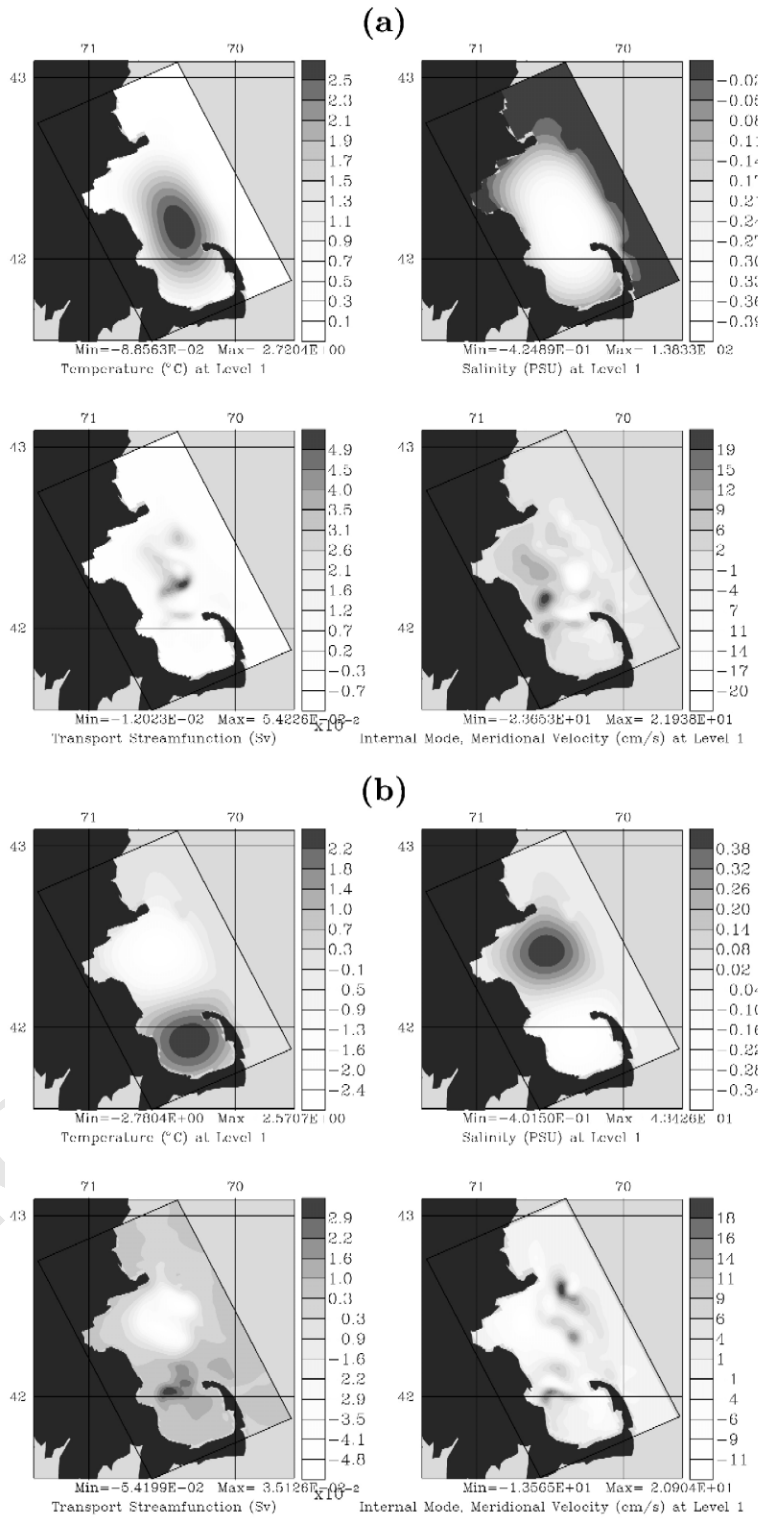
(a)
Min=−8.8563E−02 Max= 2.7204E+00
Temperature (°C) at Level 1
Min=−4.2489E−01 Max= 1.3633E−02
Salinity (PSU) at Level 1
Min=−1.2023E−02 Max= 5.4226E−02
x10−2
Transport Streamfunction (Sv)
Min=−2.3653E+01 Max= 2.1938E+01
Internal Mode, Meridional Velocity (cm/s) at Level 1
(b)
Min=−2.7804E+00 Max= 2.5707E+00
Temperature (°C) at Level 1
Min=−4.0150E−01 Max= 4.3426E−01
Salinity (PSU) at Level 1
Min=−5.4199E−02 Max= 3.5126E−02
x10−2
Transport Streamfunction (Sv)
Min=−1.3565E+01 Max= 2.0904E+01
Internal Mode, Meridional Velocity (cm/s) at Level 1

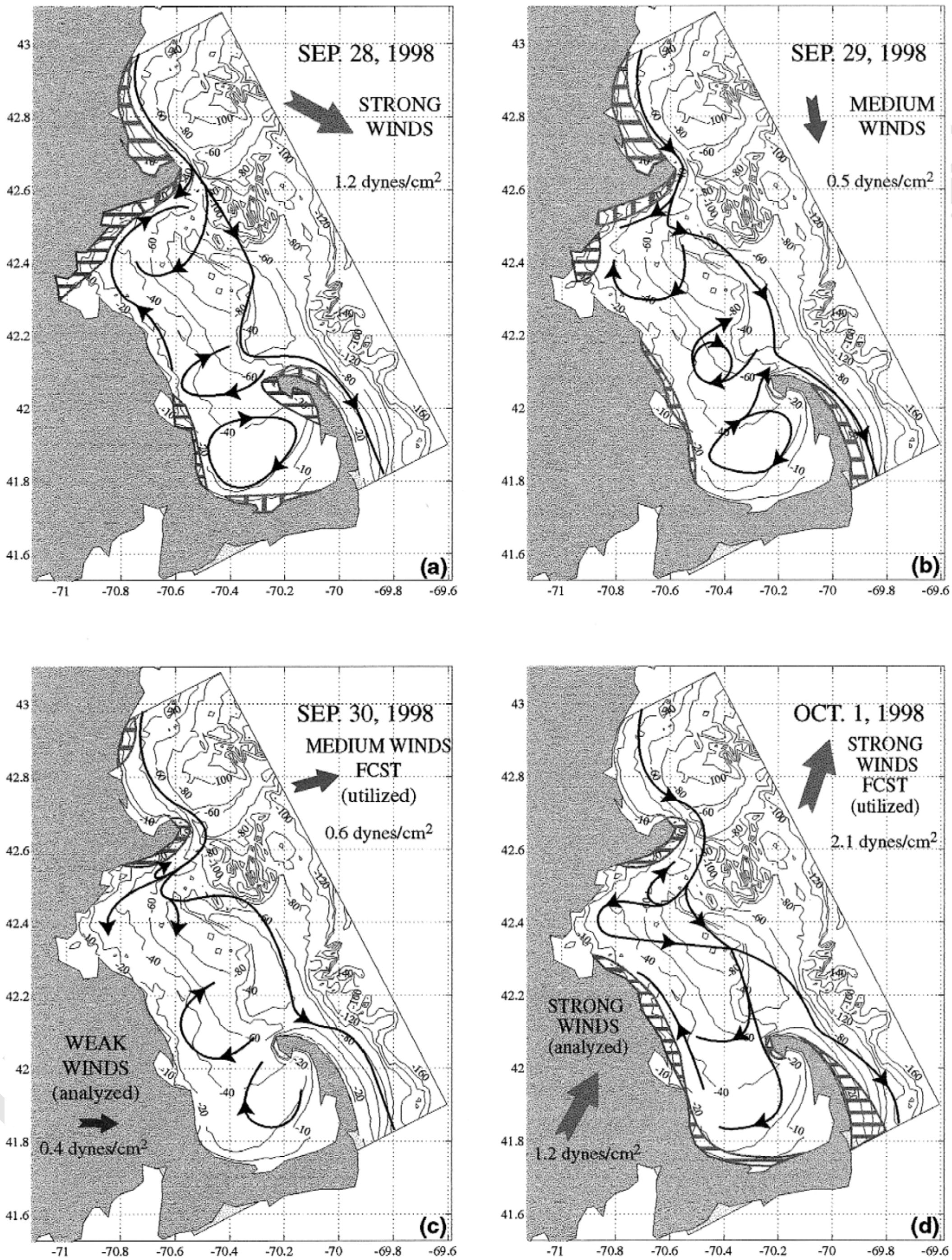

Fig. 5. As for Fig. 3a, but for the period Sep. 28–Oct. 1. Starting on Sep. 30, the atmospheric forcings employed are forecasts; the analyzed winds are drawn in the bottom left corners only for reference.

local structures of the currents, however, depend on the relative strength of inertia, topographic effects, and internal dynamics. The flow evolution is thus described next, going day by day from the global wind forcing to the local features of the circulation.

The northeastward (to the northeast) winds of Sep. 27 (Fig. 3), amplifying to the east-southeast by Sep. 28 (Fig. 5a), lead to an upwelling along the northern coast of Mass. Bay, from Boston Harbor to Gloucester (Fig. 1), a process also observed by Kangas and Hufford (1974). In this region, an anticyclonic gyre is forming in the top layers of the thermocline, in accord with the input of negative potential vorticity (squeezing of these layers). This anticyclone is fed by a buoyancy-driven (upwelled water), clock-wise rim current whose origins are at the anticyclonic vortex located just north of Cape Cod Bay (Fig. 5a). Inside of Cape Cod Bay, the Sep. 27–28 rotation of the winds from northeastward to east-southeastward has closed the Bay-wide anticyclone, with velocities larger than 5 cm s^{-1} (local maximum at 10 m is about 12 cm s^{-1}). The internal effects of these winds are also strong enough to straighten the offshore meanders and amplify the inshore meanders of the Gulf of Maine coastal current (e.g. around Stellwagen Bank, compare Figs. 3 and 5a).

Outside of Mass. Bay, on Sep. 28 (Fig. 5a) and 29 (Fig. 5b), the strong east-southeast winds, turning to medium south-southeast, strengthen the Gulf of Maine coastal current (the corresponding barotropic transport grows from 0.08 Sv on Sep. 27 to 0.14 Sv on Sep. 29). Northeast of Cape Ann and southeast of Provincetown (Fig. 5b), the coastward Ekman transport drives a downwelling along the sloping topography (by mass conservation). This surface Ekman layer forcing corresponds to a convergent barotropic deformation field (blocked by the coast), which accelerates the Gulf of Maine coastal current and enhances the initially weak horizontal density gradient into a strong coastal front. In the open-ocean, an analogous process is generally referred to as frontogenesis (Hoskins and Bretherton, 1972; MacVean and Woods, 1980); a peculiarity of the coastal set-up is that only one side of the deformation field is necessary. In general, as one crosses the present coastal fronts, the ageostrophic vertical velocities change sign. Together with small horizontal across-front velocities, they form vertical cells, similar to these of open-ocean fronts (Spall, 1995, 1997), where the wind favors coastal downwelling, a coastal front forms and, on the offshore side of the front, there is usually a local increase of upward vertical velocity[4], and inversely.

As the coastal current velocity increases by the above wind effects, so does the Coriolis force and veering to the right after Cape Ann, just inside of Mass. Bay (see Fig. 5a,b). This veering is reenforced by the west-southwest Ekman transport, leading to a branch of the coastal current entering northern Mass. Bay (Fig. 5b) and a downward tilt of the thermocline south of Cape Ann. Locally, along the bottom near the coast, the effects of the sustained winds can extend down to about 50-m depth (see Fig. 8b hereafter). The anticyclone in northern Mass. Bay (Fig. 5a) is therefore being destroyed (Fig. 5b). In southern Mass. Bay, the two anticyclones weaken mainly because of internal processes (e.g. mixing) and external medium winds which force a small downwelling and weak southward coastal current from Scituate to Sandwich (Fig. 1).

On Sep. 30 (Fig. 5c), the intrusion in northern Mass. Bay in still strengthening, even though the wind is not favorable locally. This is because the wind is too weak; locally, inertia dominates[5]. In southern Mass. Bay, the two anticyclones continue to weaken. At the outer boundary of Mass. Bay, meanders of the Gulf of Maine coastal current are forming, in response to topographic and thermal-wind forcings.

On Oct. 1, the wind is forecasted to be strong, north-northeast (Fig. 5d). Outside Mass. Bay, in the

[4] For example, on Sep. 28–29, on the offshore side of the front near Cape Ann, upwelling occurs, e.g. see vertical velocity in Fig. 8a hereafter. For simplicity, in Figs. 3 and 5, vertical motions are however only represented on the coastal side of such fronts.

[5] On Sep. 30, the order of the acceleration due to inertia is $(U^2/L) = 0.4^2/5\times10^3 = 3.2\times10^{-5}$ m/s^2, while that due the winds is $(\tau/\rho_0 h^e) = 0.6$ dyn/cm$^2 \times 10^{-5} \times 10^4/1025$ kg/m$^3 \times$ 5 m $= 1.2\times10^{-5}$ m/s^2, which is near three times smaller. In the above, U and L are the local horizontal speed and space scale, respectively (e.g. Section 5.1.1 and Fig. 8a for values), τ is the wind-stress (e.g. Fig. 5c), ρ_0 is a reference density and h^e is the order of the Ekman depth (e.g. Section 3.2).

inflow and outflow regions, this wind-forcing tends to reverse the effects of the Sep. 28–29 period and so restore by upwelling and frontolysis a relatively flat thermocline at the coast. The barotropic amplitude of the Gulf of Maine coastal current is in fact reduced to 0.09 Sv, which is close to the Sep. 27 value of 0.08 Sv (Section 5.1.1). Near Cape Ann, the sustained Ekman transport during Sep. 30–Oct. 1 displaces the Gulf of Maine inflow offshore southeastward, and a small anticyclonic recirculation cell is created by upwelling at the coast, north of the inflow (Fig. 5d). Inside the Bay, the strong southerly Oct. 1 winds create a tendency towards a Bay-wide anticyclonic circulation. Upwelling occurs from Boston to Cape Cod (past Barnstable), in accord with previous local observations of Woodcock (1984), and a northward coastal current is building up. These wind-forced motions compete with the remaining inertia of the cyclonic intrusion in northern Mass. Bay (Fig. 5b,c). By mid-day (Fig. 5d), this competition results to a branch of the coastal current that penetrates northern Mass. Bay, loops around the exit in a diagonal to the southeast.

5.2.2. Dominant variability covariance forecasts for Oct. 1: standard deviations

The square-roots of the diagonal elements of $\mathbf{B}^p$ forecast for Oct. 1 are illustrated by Fig. 6. Within this 3D and multivariate field, the surface standard deviations of the T, S, $\sqrt{\hat{u}^2 + \hat{v}^2}$ and ψ variability are plotted. They are overlaid with two ship tracks which illustrate the quantitative design of the sampling strategies (Section 3.1).

The surface temperature standard deviations (Fig. 6a) are large along an axis going from Sandwich to the center of the open-boundary of Cape Cod Bay. This area of large T variability is maintained down to about 30 m, with the peculiarity that as depth increases from 0 to about 10 m, its horizontal maximum gets closer to the coast towards Sandwich, while from 10 m to the bottom, it moves back away from the coast. This 3D pattern is reminiscent of the coastal upwelling/downwelling occurring in this region, and agrees with the fact that large temperature shear and mixing are expected at the boundaries of the corresponding jets and fronts (see Figs. 3 and 5).

Another region of dominant T variability is at the northern coast of Mass. Bay. This local high is limited to the surface layers between 0 and 10 m. It is mainly associated with recent variations in the local upwelling/downwelling conditions, Ekman layer mixing and internal advection (see Figs. 3 and 5). The surface salinity variability forecast (Fig. 6b) is also large in this northern region, for the same reasons. In the rest of domain, its largest values are not at the open-boundary of Cape Cod Bay as for T, but near the highly variable anticyclone at the north of Cape Cod Bay (Figs. 3 and 5). This local high in S standard deviations extends below the thermocline, down to about 30 m, and around the “elbow” of Stellwagen Bank (Fig. 1). As depth increases, the local dominance of S over T decreases (the non-dimensional standard deviations of T and S become similar). Nonetheless, over the full domain, the discrepancies between the T and S standard deviation patterns (e.g. Fig. 6a,b) show the importance of multivariate effects in Mass. Bay.

The forecast for Oct. 1 of the surface internal speed variability (Fig. 6c) presents more anisotropy and smaller horizontal scales than the surface tracer variabilities. The internal velocity variability is indeed largest mainly along the frontal zones and filaments of highest forecast variations in the Bay; with Figs. 3 and 5 in mind, consider for example in Fig. 6c, the inflow from the Gulf of Maine, the anticyclone to the north of Cape Cod Bay and the western side of the gyre within Cape Cod Bay. Distinctive properties of the barotropic transport standard deviations (Fig. 6d) are that they are largest along the meanders of the Gulf of Maine coastal current, often following topography (Fig. 1), and that they usually increase with depth. An important result is that the regions and variables of high standard deviations clearly correspond to the features and variations identified in Section 5.2.1. In fact, the standard deviation forecasts were used to focus on the features of high variability and carry the analysis of Section 5.2.1.

The standard deviation forecasts were also useful for the real-time design of the sampling strategies (overlaid in Fig. 6). For example, the zigzag sampling pattern (14 CTDs) to the north of Cape Cod Bay was selected late on Sep. 29, within a set of pre-determined tracks and carried out on Sep. 30 during daylight (see Appendix C for timings). The

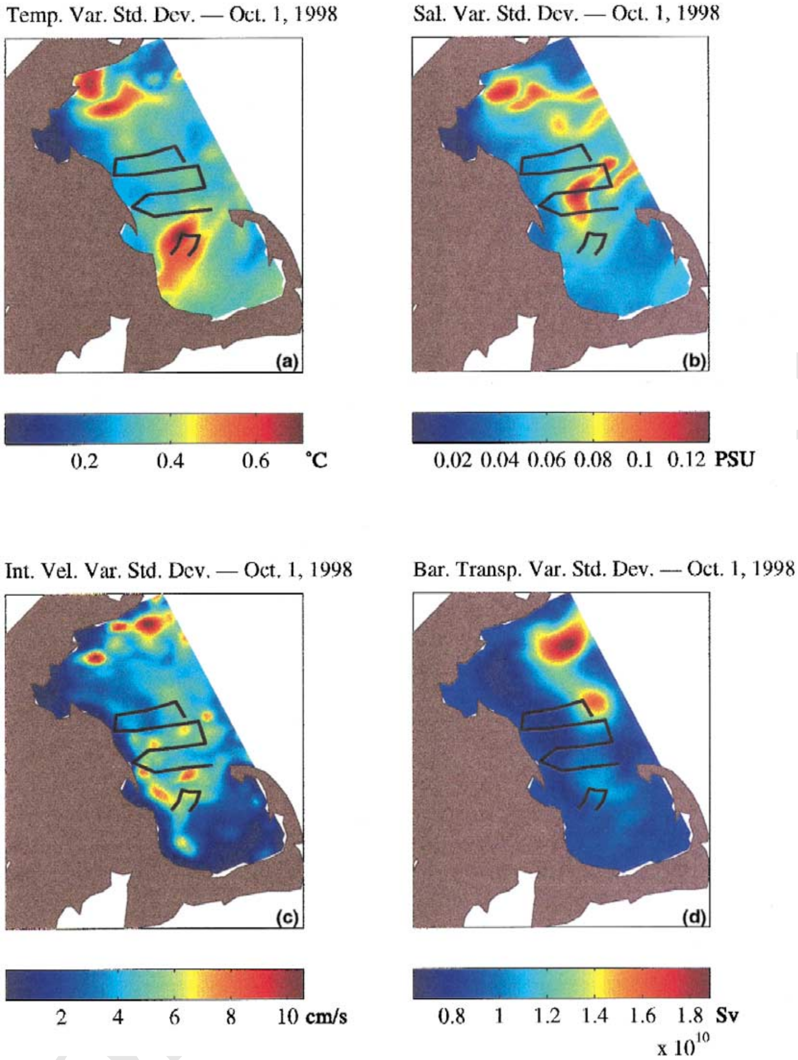

Fig. 6. Surface standard deviations of the variability forecasts for Oct. 1, overlaid with the sampling tracks carried out on Sep. 30 and Oct. 1.

criteria to select this pattern were the: (i) need to update the inflow–outflow of Cape Cod Bay, an area not visited for some time; (ii) first estimate late on Sep. 29 of the standard deviation forecast for Oct. 1, already indicating large variabilities in salinity and surface internal velocities in this area (Fig. 6b,c); and (iii) need to use a pre-determined track because of time constraints and risk of miscommunication. The U-shaped sampling pattern overlaid at the entrance of Cape Cod Bay was designed late on Sep. 30 (Appendix C) and carried out on Oct. 1. The design criteria involved the: (i) forecast for Oct. 1 of the local high spot in temperature and velocity variations (see Fig. 6a,c,d); and (ii) increasingly bad weather (see Fig. 5d) and need for instrument testing, which both constrained the survey to be short and within Cape Cod Bay.

5.2.3. Dominant variability covariance forecasts for Oct. 1: covariance eigenvectors

The forecast for Oct. 1 of the dominant variability eigenvectors, columns of $\boldsymbol{E}^*$ in Appendix A, Eq. (A5) are illustrated by Figs. 7–14. Each vector is of dimension n, corresponding to the multivariate and three-dimensional state variables $\boldsymbol{x}$ in Appendix A, Eq. (A1a). For efficiency, when showing such a vector, the type and depths of the variables plotted are chosen so as to illustrate the largest amplitudes and possible dynamical meaning.

By definition, these eigenvectors correspond to regions and processes of dominant variability on Oct. 1. Because of the memory contained in Appendix A, Eqs. (A4a)–(A5), they also relate to variations of fields before and after Oct. 1 (see Appendix B), as did the standard deviations. Using the dominant eigenvectors as a guide, we were thus able to identify and focus on critical snapshots and tendencies (time-differences) of physical fields, and so locate interesting dynamical aspects of the 4-day simulation. Results are presented next, vector by vector.

5.2.3.1. First eigenvector. The first vector (Fig. 7) indicates a direction in the variability space that is associated with a displacement of the Gulf of Maine coastal current offshore from Cape Ann, with an increase of the inflow offshore and a decrease of the inflow near the coast. With the sign of the vector plotted in Fig. 7 (the sign is arbitrary), note that it points to a displacement shoreward, towards Cape Ann (i.e. a decrease offshore).

Horizontal maps of the T, S and $\hat{u}$ components at 20 m and of the ψ component are shown in Fig. 7a. The depth of 20 m was chosen for T, S and $\hat{u}$, because near Cape Ann, it is in the upper layers of the pycnocline and logically around the depths of maximum amplitudes for this vector. Notice first that T and S are in opposition of phase, hence adding effects on density. Focusing for each variable on the lobe along the northern coastline (near 20 m, these lobes are the primary ones, with the largest magnitudes), notice the upward dome of the pycnocline, with a local low in T and high in S, the main

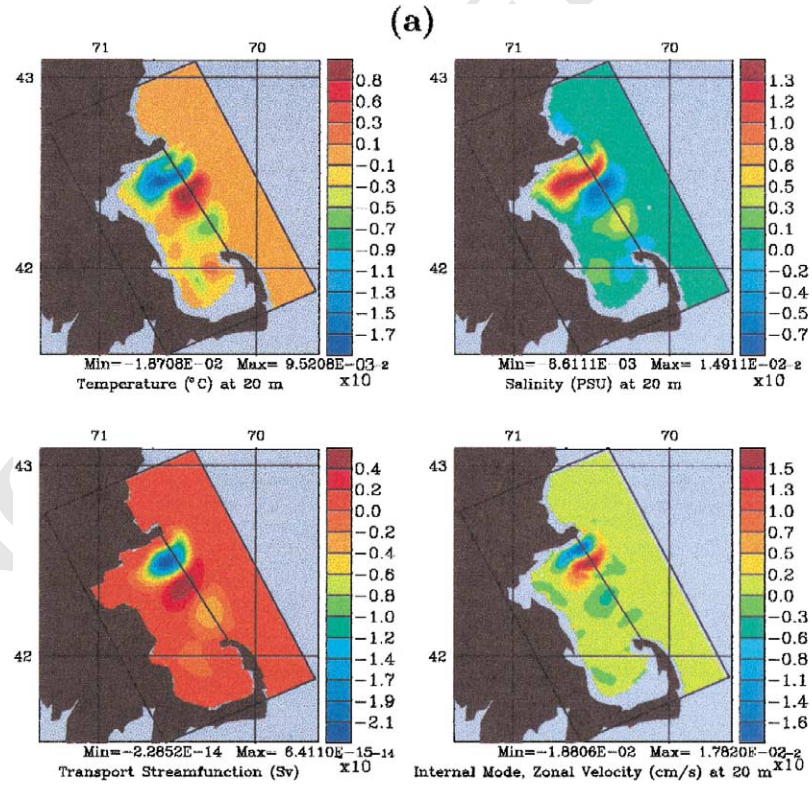

Fig. 7. Four model-day forecast of the first variability eigenvector for Oct. 1. The labels indicated the components shown. All values are non-dimensional. (a) Horizontal maps at 20 m. (b) Cross-sections (0–80-m depth) along the outer boundary of Mass. Bay, from Race Point on the left, to Cape Ann on the right (section position is drawn on (a)).

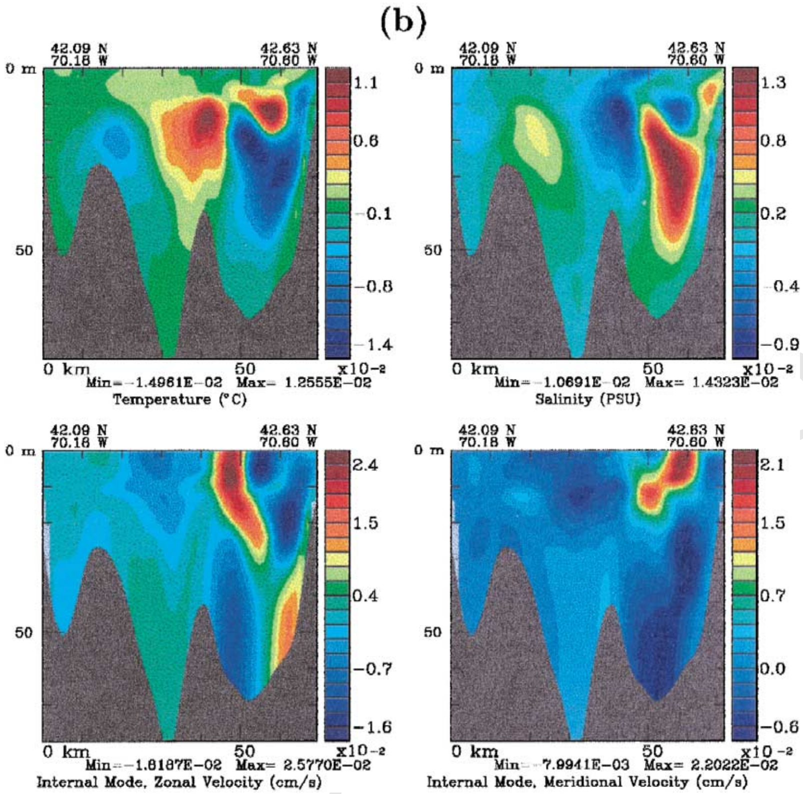

Fig. 7 (*continued*).

cyclonic cell for ψ and the corresponding dipole in $\hat{u}$, with an inflow at the coast and outflow offshore. By continuity and inertia, offshore from these dominant lobes, there are lobes of opposite sign, but of lesser amplitudes at 20 m (Fig. 7). They point to a downward motion of the pycnocline, with a local high in T and low in S, an anticyclonic cell for ψ and an anticyclonic dipole in $\hat{u}$ (of weak inflow side at 20 m). Combining these secondary lobes with the primary ones leads to dipoles in T, S and ψ, and a tripole in $\hat{u}$. They allow to explain shoreward/offshore displacements of the Gulf of Maine coastal current and the possible creation of adjacent mesoscale recirculation cells.

This first vector has strong extrema in the pycnocline, but its vertical structure is not uniform. For example, consider the cross-sections in its T, S, $\hat{u}$ and $\hat{v}$ components along the outer boundary of Mass. Bay (Fig. 7b). In northwestern Mass. Bay, above the North Passage (Fig. 1), there is a local high in T and low in S near 12 m. With the opposite sign, it can indicate a local upwelling and an inflow of cooler and fresher water from the north of Cape Ann and Merrimack river (Geyer et al., 1992). In the surface Ekman mixing-layer, T and S have more scales, reflecting the local variations of the mixing, atmospheric flux and advective effects. However, the maximum amplitudes are there much less significant, three to six times smaller than in the pycnocline (e.g. at 20 m in Fig. 7a). In these surface layers, the $\hat{u}$ and $\hat{v}$ components (Fig. 7b) have similar signs and patterns than at 20 m, but their amplitudes are slightly larger (maximum near 5 m), in accord with a near thermal-wind balance. Flipping the sign of the vector, note the $\hat{v}$ convergence above the northern slope of Stellwagen Bank from 0 to 25 m, hence the strengthening of the Gulf of Maine inflow at that location (see $\hat{u}$ in Fig. 7b). The $\hat{u}$ and $\hat{v}$ zero-crossings are around 30 m. Below, the $\hat{u}$ and $\hat{v}$ extrema are near 50 m, but their amplitudes are two to five times smaller than their opposite at the top of the pycnocline.

Guided by the first vector forecast for Oct. 1, a more detailed analysis of some events and vertical processes that occurred near North Passage during the 4 days of simulation is now given. The "central forecast" is chosen for sample path realization of Appendix A, Eq. (A1a). During Sep. 27, the first vector (Fig. 7) is not strongly excited: the formation of the anticyclonic gyre by coastal upwelling is mainly limited to the north-western side of Mass. Bay, near Broad Sound (Figs. 3 and 5a). Getting closer to Oct. 1, from Sep. 28 to the end of Sep. 29, the correlation increases. The excitation of the first vector is on volume-average negative: the wind-forced convergent deformation field, west-southwest Ekman transport, Coriolis force and inertia combine to strengthen the Gulf of Maine inflow in northern Mass. Bay and enhance the density front by coastal downwelling (see Section 5.2.1 and Fig. 5a,b). This is illustrated by the cross-sections of Fig. 8 (same location as these of Fig. 7b). The density anomaly σ_t, salinity S, total zonal velocity u and vertical velocity w of the central forecast on Sep. 29 are plotted in Fig. 8a. The variations of the central forecast T, S, $\hat{u}$ and $\hat{v}$ between Sep. 29 and 28 are in Fig. 8b, allowing direct comparisons with the state variables of Fig. 7b. One clearly notices the strengthening of the Gulf of Maine inflow (see negative u in Fig. 8a and $\hat{u}$ tendency in Fig. 8b), and the enhanced density front by downwelling at the coast (see w in Fig. 8a, and T and S tendencies in Fig. 8b). On average, these Sep. 28–29 facts are represented by the patterns of Fig. 7b (e.g. flipping the sign of the vector, see the remanents of coastal downwelling in T and S of Fig. 7b). However, the weak secondary lobes in the 1-day tendencies (Fig. 8b) and corresponding fields (in Fig. 8a, see the oscillations of the

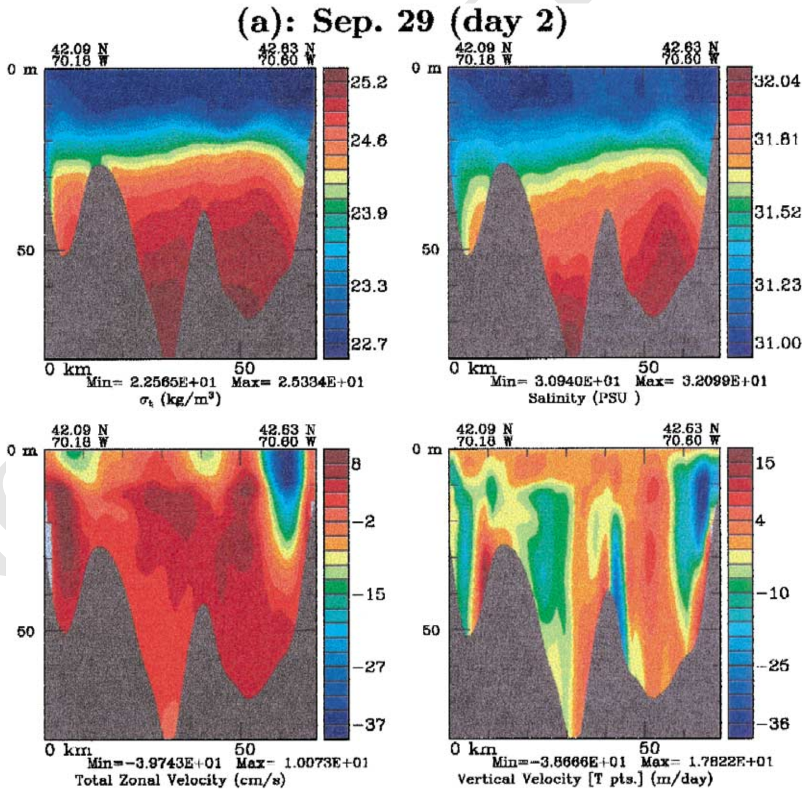

Fig. 8. Vertical cross-sections in forecast fields along the outer boundary of Mass. Bay, at the same location as on Fig. 7b. (a) Fields on Sep. 29 (day 2 of central forecast). (b) Differences between the T, S, $\hat{u}$ and $\hat{v}$ fields of Sep. 29 (day 2 of central forecast) and Sep. 28 (day 1 of central forecast).

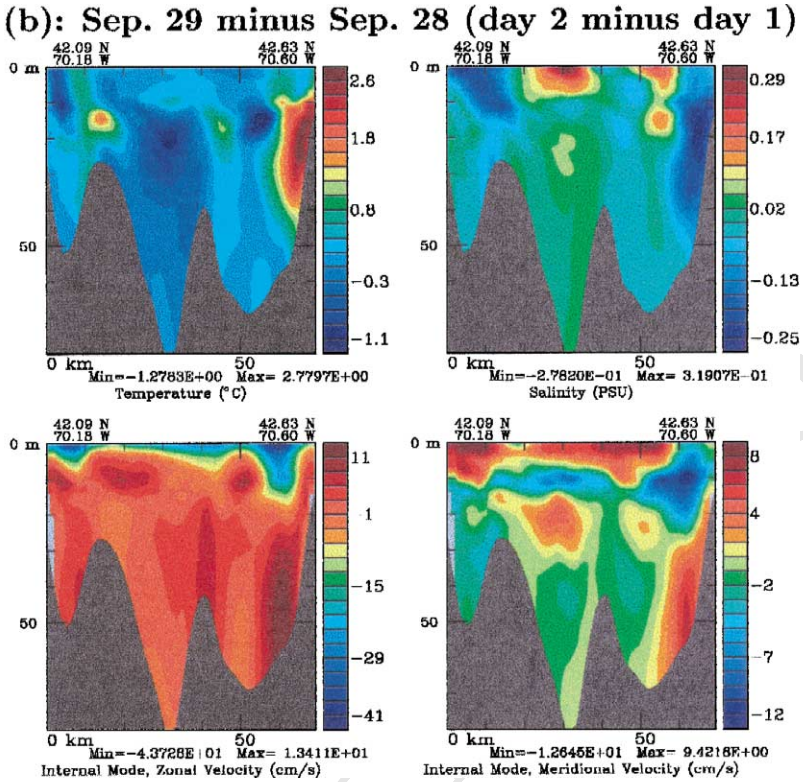

Fig. 8 (*continued*).

pycnocline near $\sigma_t = 23.5$ and halocline near $S = 31.3$, and the highs and lows in u and w) are not in phase with the patterns of Fig. 7b. They are closer to the coast, in accord with the position of the Gulf of Maine inflow on Sep. 29 (Fig. 5b): for example, at the surface, the velocity patterns of Figs. 8b and 7b are close to quadrature of phase.

Starting on Sep. 30 and increasing on Oct. 1 (Fig. 5c,d), the relationships with the first vector are logically the strongest. As shown by the cross-sections of Fig. 9, the excitation of the first vector is negative (e.g. compare Fig. 9b with Fig. 7b), and involves the main $\hat{u}$ tripole and all of the T, S and ψ dipoles (e.g. at 20 m, the secondary extrema are above the northern slope of Stellwagen Bank, about 25 km from Cape Ann, almost as in Fig. 7). The pycnocline and halocline are being flatten at the coast toward a restoration of the initial Sep. 27 conditions (see Figs. 9a,b and 7b). Even though the $\hat{u}$ and $\hat{v}$ tendencies contain the effects of the wind on the surface currents (Fig. 9b), the velocity patterns extracted by the first vector are also visible. The Gulf of Maine inflow is clearly being displaced offshore (see u in Fig. 9a and $\hat{u}$ tendency in Fig. 9b). A surface mesoscale anticyclonic recirculation cell is created at the coast (in the Ekman layer, see spots of $\hat{u} \geq 0$ and $\hat{v} \leq 0$ in Fig. 9b, and of $\hat{u} \leq 0$ and $\hat{v} \geq 0$ in Fig. 7b). Finally, the vertical velocities are reversed at depths, across the whole section (compare w of Figs. 8a and 9a), in accord with a reduction of the Gulf of Maine inflow in Mass. Bay by Bay-wide frontolysis (Section 5.2.1). The interaction of the wind-response, pycnocline and topographic effects can thus lead to connected patterns along the outer boundary of Mass. Bay, as suggested by the first vector. Note that the wind forcings and corresponding adjustments illustrated by Figs. 7–9 also induce oscillations close to the Coriolis frequency (not shown) near the coastal front and pycnocline, and thus to inertial pumpings (Price, 1983; Lee and Niiler, 1998). When winds change direction, these oscillations and vertical velocity perturbations reverse sign, as estimated in Figs. 8 and 9. Vertical velocity patterns are not maintained.

The above analysis of processes that occur near North Passage is confirmed by simulated Lagrangian drifters (Fig. 10). All drifters are deployed at t_0 on Sep. 27 along the outer boundary of Mass. Bay. They all keep a constant depth of 10 m. Describing trajectories from north to south along the deployment locations, the drifter released at the coast of Cape Ann is slowly advected westward, within the coastal boundary layer on the northern edge of the Gulf of Maine inflow, except on the last day during which winds strongly reverse (see Fig. 5d). The second and third drifters (next ones to the south) are initially in the outflow branch of a mesoscale meander of the coastal current (see Fig. 3 above North Passage), but they reverse course at the end of Sep. 28 (day 1) and at the beginning of Sep. 30 (day 3), respectively. For the second drifter, this is in accord with the strengthening of the Gulf of Maine inflow near the coast of Cape Ann during Sep. 28–29 (Figs. 5a,b and 8). For the third drifter, this agrees with the patterns of Figs. 7 and 9, which revealed the details of a displacement of the Gulf of Maine inflow offshore, starting on Sep. 30 (Fig. 5c,d). Finally, the other drifters show that during Sep. 27–Oct. 1, the meanders of the Gulf of Maine coastal current are estimated to decrease their intensity as the distance from Cape Ann increases, in accord with the decaying amplitudes of the patterns of the first eigenvector (Fig. 7).

5.2.3.2. Second eigenvector. The second vector (Figs. 11 and 12) mainly indicates a direction in the variability space that corresponds to a coastal upwelling mode from Barnstable Harbor to Gloucester. This is in response to the north-northeastward winds that

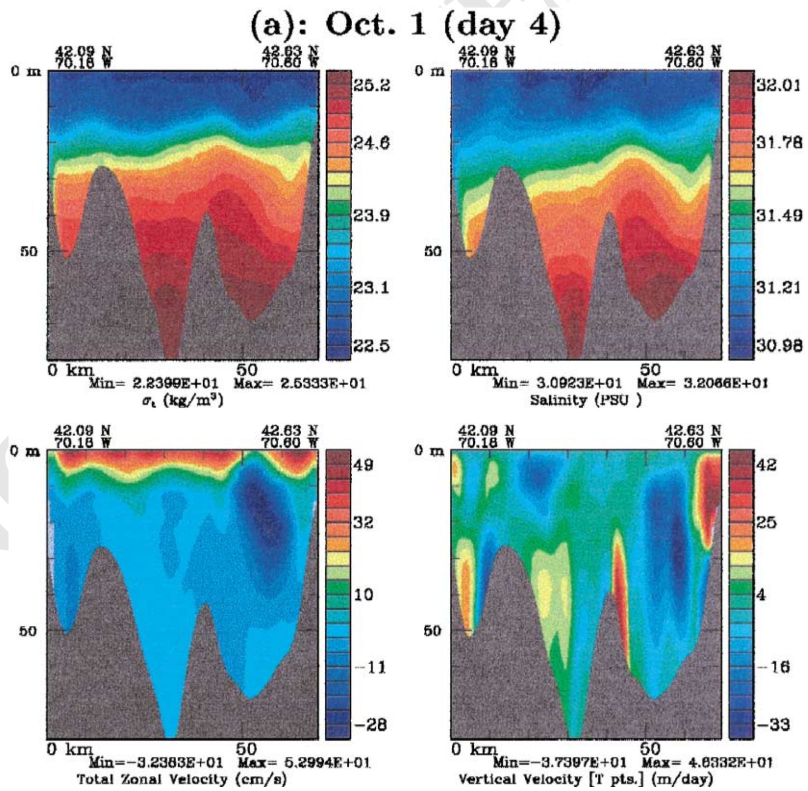

Fig. 9. Vertical cross-sections as on Fig. 8, but for different dates. (a) Fields on Oct. 1 (day 4 of central forecast). (b) Differences between T, S, $\hat{u}$ and $\hat{v}$ fields on Oct. 1 (day 4 of central forecast) and Sep. 29 (day 2 of central forecast).

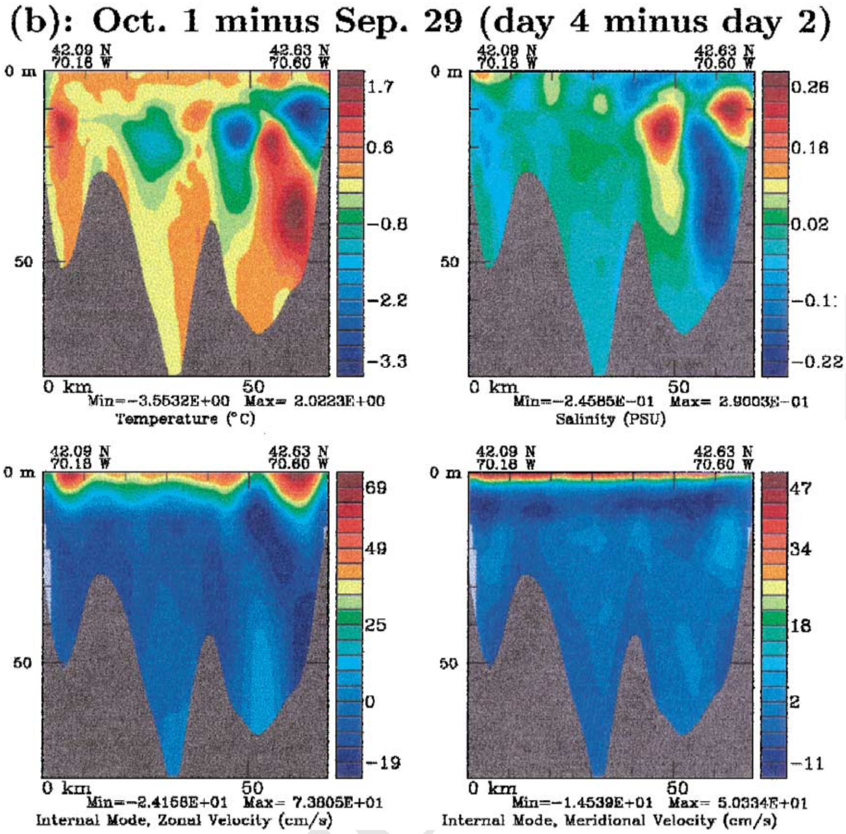

Fig. 9 (*continued*).

occur on Sep. 27 and during Sep. 30–Oct. 1 (Figs. 3 and 5c,d). For the sign opposite to that of Figs. 11 and 12, the vector also relates to some of the downwelling patterns that south-southeastward winds force south of Boston, as it occurs during Sep. 28–29 (Fig. 5a,b).

Focusing on the temperature component, horizontal T maps are plotted in Fig. 11, at depths increasing from the surface to 20 m (T suffices because over the upwelling regions, T and S were found closely in opposition of phase). In the Ekman mixing-layers (first level to 10 m in Fig. 11), from Boston to Sandwich, the vector shows an extended cooling by strong wind-induced advection of cold waters from the shore and by vertical mixing. The extent of this cooling is widest to the northeast of Scituate, where it reaches the center of the Bay. At these locations, and along Cape Ann from Salem to Gloucester, cold waters are exposed to the surface indicating a full upwelling (Csanady, 1977). In the surface layers near Boston Harbor, the amplitude of the T component is weak because this shallow area is relatively well mixed by wind and tidal forcings, even before Sep. 27 (one needs to reach 10 m, near Broad Sound, to see a significant T gradient). Several vertical properties of the upwelling are also captured by the first vector. For example, the horizontal extent of the upwelling narrows as depth increases (e.g. compare T at 5 and 20 m) and the largest amplitudes are usually near the pycnocline (e.g. compare T at level 1 and 10 m).

Mainly because of the orthogonality constraint, some variations that are likely not physically connected to coastal upwellings are also explained by this second vector. For example, for the T component (Fig. 11), the influence of the first vector is felt above the North Passage and along the outer boundary of Mass. Bay: the amplitudes of patterns there

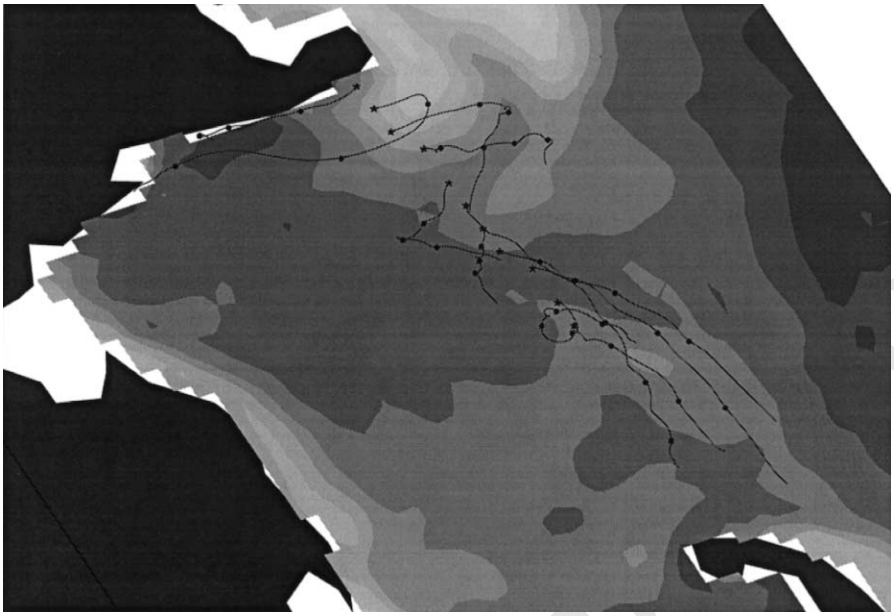

Fig. 10. Numerically simulated drifter trajectories at 10 m, overlaying the 10 m temperature forecast for Oct. 1. A total of 11 simulated drifters were released at t_0 (Sep. 27, 12 GMT), along the outer boundary of Mass. Bay. The stars indicate the simulated deployment sites. For each trajectory, every day starting from t_0, a full circle is drawn to indicate daily intervals.

(overall, warming and downwelling) should likely be smaller if they were only related to the physics of the coastal upwelling (see Fig. 13 hereafter). Similarly, the positive T lobe in the surface layers of western Cape Cod Bay is likely there because of the orthogonality with the fifth vector (not shown): its amplitude would be larger for a significant physical correlation with the coastal upwelling.

The barotropic transport component of this second vector is plotted in Fig. 12a. It clearly confirms a field observation (Section 5.2.1): strong, north-northeastward winds tend to create a Bay-wide anticyclonic vertically averaged circulation, by combination of wind-driven surface currents with upwelling-induced buoyancy-driven currents. This is an important result for the real-time modeling experiment. Note again the influence of the orthogonality with the first vector, as shown by the weak cyclonic recirculation cell along Cape Ann.

The cross-sections of Fig. 12b illustrate the vertical structures of this second vector near the position where the coastal upwelling pattern has maximum width (Fig. 11). In the upwelling zone, the T and S components are closely in opposition of phase, combining each other in density. Along the sloping bottom, upwelling effects begin in this cross-section near 40-m depth. They are maximum at the coast and in the upper layers of the pycnocline. Away from the coast, in the Ekman mixing-layer, the amplitudes of the T and S components are substantially smaller. An offshore downwelling pattern above Stellwagen Basin is also part of this vector (in Fig. 12b, see high in T and low in S about 30 km from the coast). These findings agree with a wind-induced, Bay-wide tilt of the pycnocline. The vector identifies a vertical cell across the Bay, extending from 10 to 40 m. Based on 2D conservation of mass, the downwelling amplitudes are somewhat too large. This is due to 3D effects (e.g. the horizontal area of the upwelling is larger than that of the downwelling), but also to the orthogonality constraint. The $\hat{u}$ and $\hat{v}$ components in Fig. 12b indicate a near thermal-wind balance, with a zero-crossing around 30 m. The $\hat{u}$ pattern has logically small values. Even though at the limit of significance, this $\hat{u}$ cross-section indicates a convergence of the northward upwelling-induced flow, in

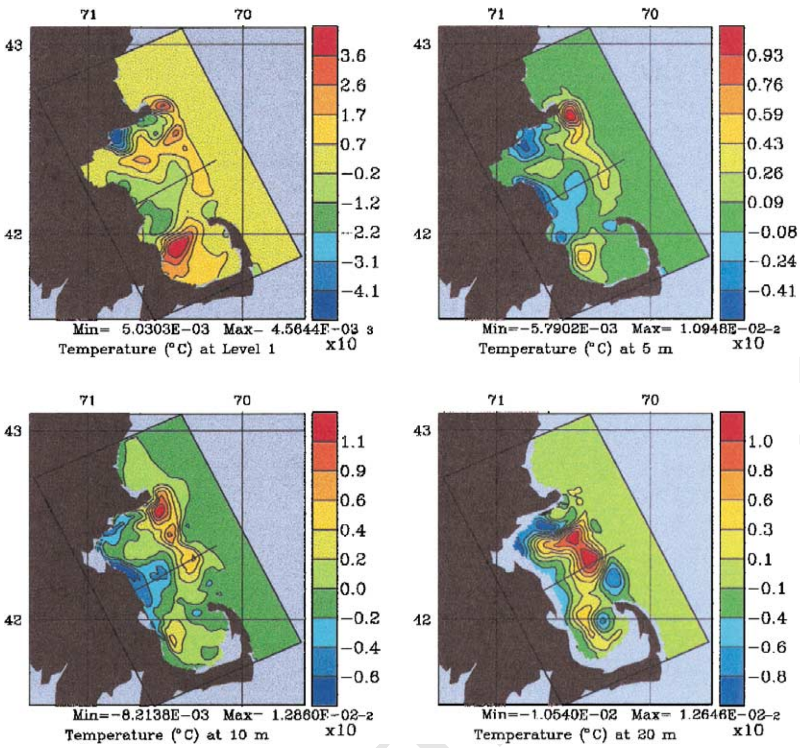

Fig. 11. Four model-day forecast of the second variability eigenvector for Oct. 1. As on Fig. 7, labels indicate the components shown, presently T at increasing depth from the surface to 20 m. All values are non-dimensional. The position of cross-sections considered on Fig. 12b is drawn.

accord with Fig. 5d. The $\hat{v}$ pattern has larger amplitudes. It shows that the northward flow is likely balanced by a southward flow on the western slope of Stellwagen Bank, in accord with the position of a branch of the Gulf of Maine coastal current forecast for Oct. 1 (Fig. 5d).

To evaluate the second vector and further illustrate how the variability decomposition can guide towards patterns and processes of largest variance, cross-sections in time-differences of central forecast fields are plotted in Fig. 13. The fields differentiated are as in Figs. 8b and 9b, but the cross-section is now across the width of Mass. Bay, as in Fig. 12b. During Sep. 28 (Fig. 13a), the excitation of the second vector is negative, in accord with coastal downwelling and relatively strong northerly winds (Section 5.2.1 and Figs. 5a,b). One clearly notices the corresponding offshore upwelling above Stellwagen Basin (see negative T, and positive S, tendencies in Fig. 13a), in good agreement with the second vector (Fig. 12b). When such an event occurs, it will strongly enhance the vertical mixing and biological activity in the region, likely surpassing the local effects of internal waves (e.g. Haury et al., 1979). The internal velocity tendencies also show similarities with Fig. 12b, especially $\hat{v}$ (Fig. 13a), despite the purely wind-induced variations in surface. From Sep. 29 to Oct. 1 (Fig. 13b), the excitation of the second vector is positive, with a coastal upwelling and cold, salty waters outcropping (Section 5.2.1 and Figs. 5c,d). However, the corresponding downwelling above Stellwagen Basin is not as strong as the second vector indicates (also true for the Sep. 30–Oct. 1 tendency, not shown). It is shallower, closer to the surface mixing-layers and to the coast (about 25 km offshore). It is also partially masked by upwellings linked to variations of the Gulf of Maine coastal current above Stellwagen Bank (see

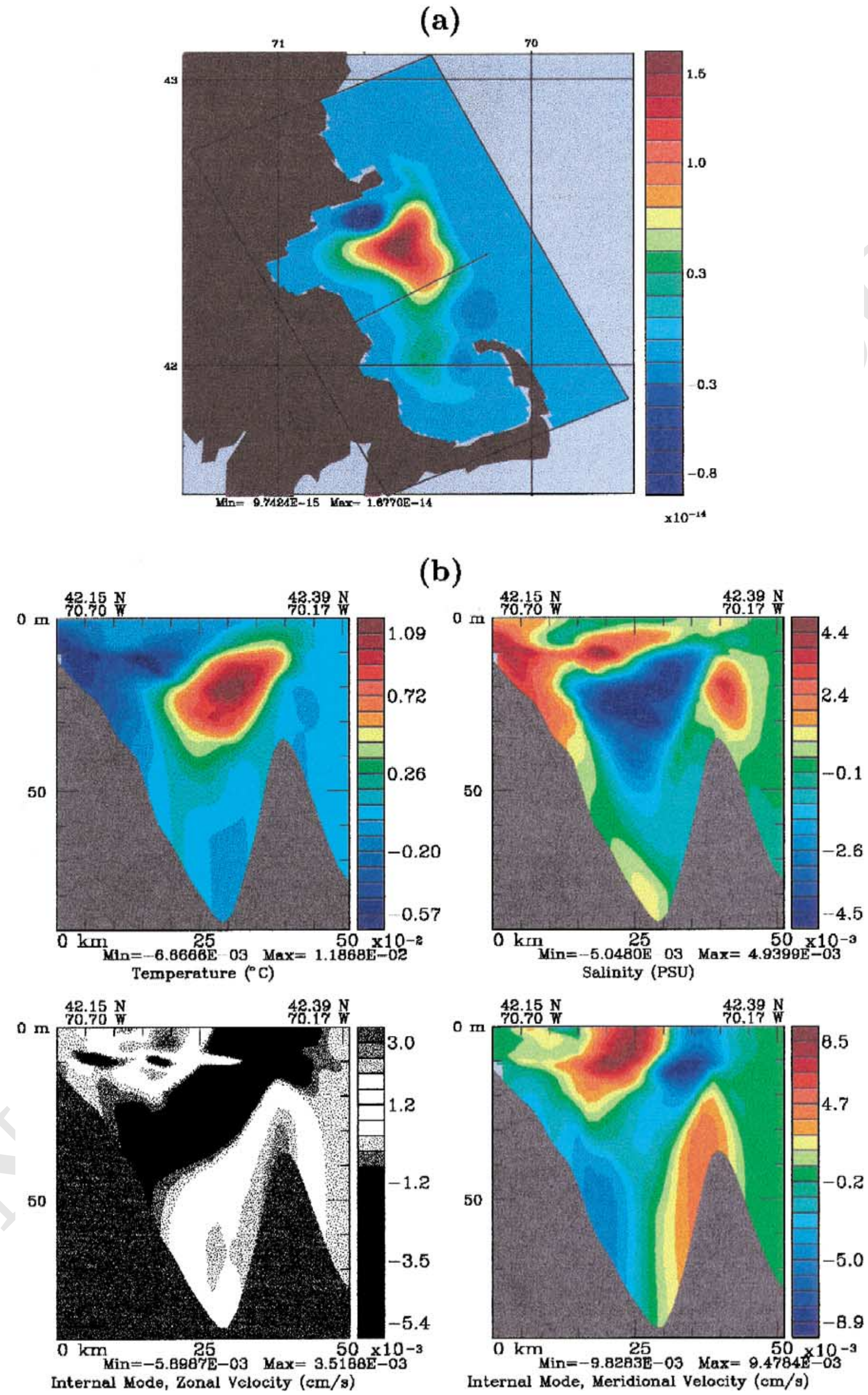

Fig. 12. As Fig. 11, except that (a) is the ψ component of the second eigenvector and (b) are cross-sections in the 3D components of this vector. The section position is drawn on panel a, cutting across the width of Mass. Bay from Scituate (on the left) to the east of Stellwagen Bank (on the right).

Fig. 5b,d). To extract the relevant velocity dynamics (Fig. 12b) from the $\hat{u}$ and $\hat{v}$ tendencies (Fig. 13b), the variability decomposition is shown helpful.

The upwelling/downwelling processes are finally illustrated by simulated Lagrangian drifters (Fig. 14). Five drifters are deployed at t_0 on Sep. 27 near Scituate, along the coastal portion of the cross-section utilized in Figs. 11–13. They are released at depths increasing with the distance from shore, from the surface to 20 m, every 5 m. They all maintain constant depth. Describing trajectories starting at the coast, the first two drifters (0 and 5 m) are on average within the Ekman depth $h^e(x, y, t)$ (Section 3.2). They agree with a spiral to the right as depth increases. During the 4 days of simulation, the surface drifter (closest to the coast at t_0) has a veering angle varying between 5° and 30° to the right of the wind (Figs. 3 and 5), as in the surface data of Geyer et al. (1992). It is vigorously advected offshore, in accord with the surface pattern of the second eigenvector (Figs. 11 and 12). The third drifter at 10 m is at the bottom or below the Ekman mixing-layer. It shows the local competition between wind and buoyancy currents (e.g. see Fig. 5a). The last two and deepest drifters, respectively at 15 and 20 m, are in the pycnocline. They respond indirectly to the strong or sustained wind events. Their horizontal motion is shoreward during coastal upwellings (Sep. 27 and Oct. 1) and offshore during coastal downwellings (Sep. 28–29), hence their rotation.

5.2.3.3. Other eigenvector and discussion. The above two eigenvectors only correspond to a piece of the variability forecast for Oct. 1. They were purposely discussed in detail because top vectors are usually the least influenced by the orthogonality constraint

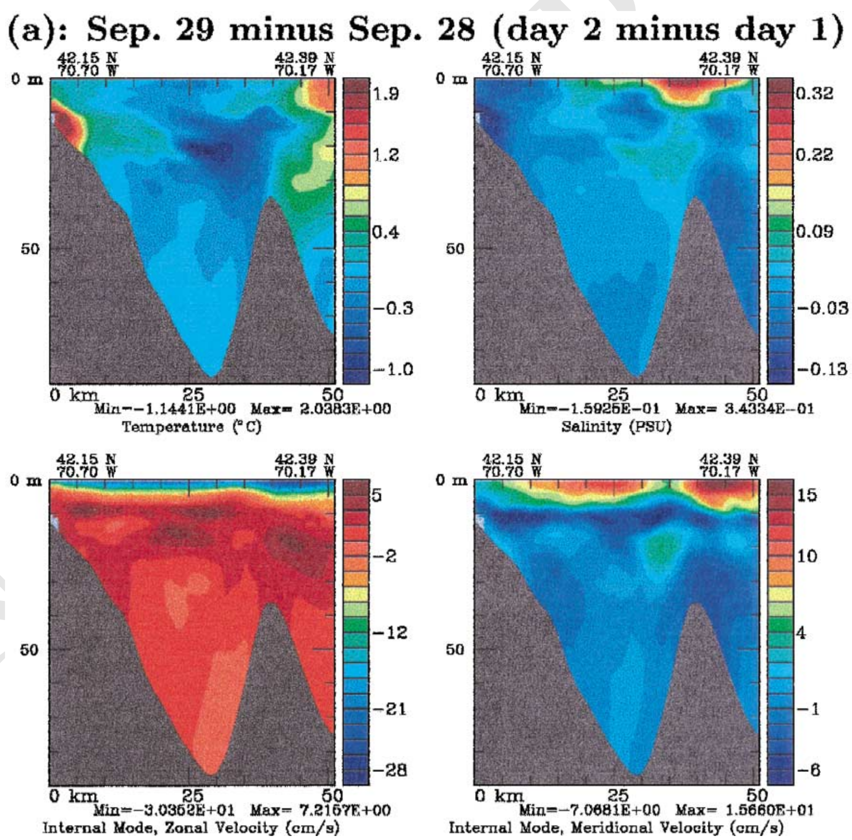

Fig. 13. Vertical cross-sections in the same central forecast tendencies as those of Figs. 8b and 9b, but from Scituate to the east of Stellwagen Bank (section position on Figs. 11 and 12a). (a) Differences between the T, S, $\hat{u}$ and $\hat{v}$ field of Sep. 29 (day 2 of forecast) and Sep. 28 (day 1 of forecast). (b) As (a), but for the differences between Oct. 1 (day 4 of forecast) and Sep. 29 (day 2 of forecast).

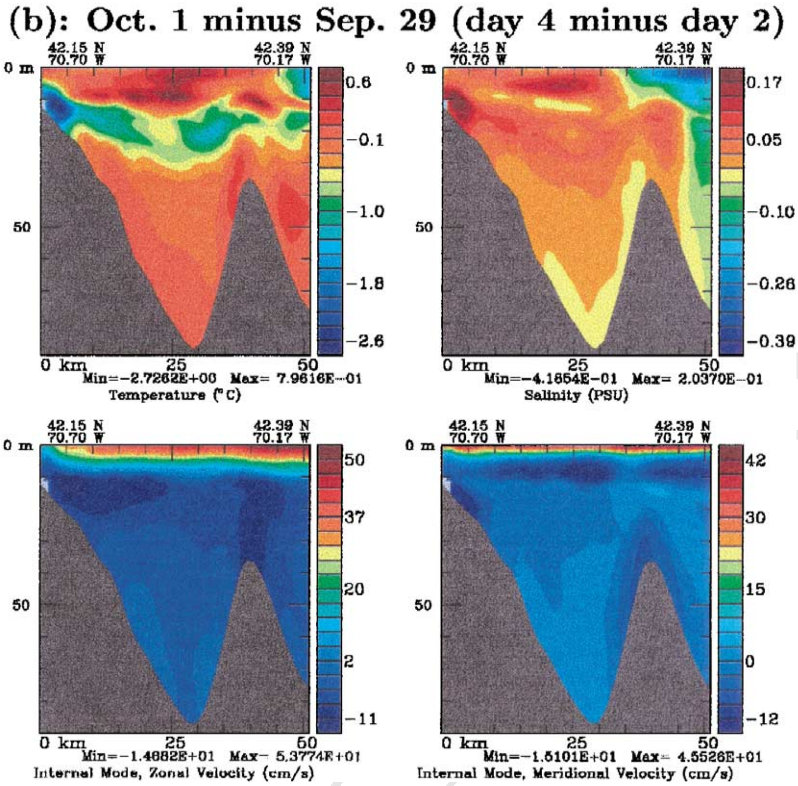

Fig. 13 (*continued*).

and thus the cleanest physically. The third vector in fact indicates a direction in the variability space physically related to the first and second vector. For its arbitrary sign, it shows: (i) a coastal downwelling pattern from Scituate to Plymouth, associated with a cyclonic transport cell in northwestern Mass. Bay; and (ii), meandering patterns of the Gulf of Maine coastal current above North Passage and along the outer boundary of Mass. Bay, with a relatively strong anticyclonic cell at the boundary of Stellwagen Basin and Stellwagen Bank (near 42.3N, 70.35W). The fourth vector is similar to the first, except that it indicates a direction corresponding to a northward displacement of the coastal current outflow, north of Race Point. The dominant amplitudes of the fifth vector point to upwelling and downwelling patterns within Cape Cod Bay, of extrema along an axis going from Sandwich to the center of the open-boundary of Cape Cod Bay. Together, these five dominant eigenvectors explain 28.3% of the three-dimensional and multivariate variance explained by the 296 Monte-Carlo forecasts. The first vector explains 7.3% of the subspace's variance, the second 5.9%, the third 5.5%, the fourth 5%, and the fifth 4.6%. The other vectors indicate additional sub-mesoscales to Bay-scales variations, e.g. related to the two anticyclones on each side of Cape Cod Bay, but their physical description requires additional machinery. Overall, the variance explained by a vector rapidly decays with the number of the vector: the 10 dominant vectors explain 43.8% of the variance, 50 dominant 77.8%, 100 dominant 89%, and 150 dominant 94.2%.

An essential property of the dominant eigenvectors is that they indicate, evolve and organize the directions in the variability space that have largest statistical significance, based on a variance measure. Their patterns are thus usually more meaningful on average than a few forecast tendencies. For example, the displacement of the Gulf of Maine coastal current according to the first vector (e.g. see $\hat{u}$ in Fig. 7b) is towards the steep northern slope of Stellwagen

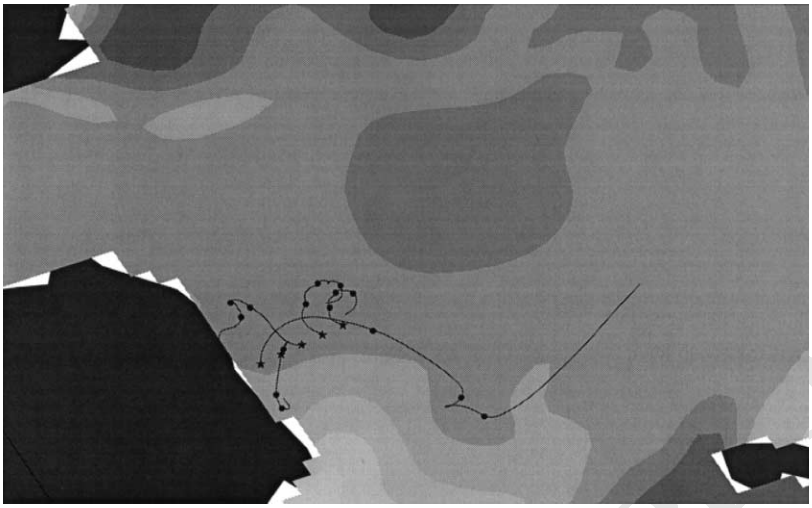

Fig. 14. Numerically simulated drifter tracks, overlaying the surface temperature forecast for Oct. 1. Five simulated drifters were released at t_0 (Sep. 27, 12 GMT), offshore from Scituate (Fig. 1), in one of the main upwelling/downwelling regions. The stars indicate the simulated deployment sites. The drifter released the closest to the coast is a surface drifter. Others are released at depths increasing with the distance from shore: the second closest to the coast is at 5 m, the third at 10 m, the fourth at 15 m and the fifth at 20 m. All drifters maintain their depth constant. For each trajectory, every day starting from t_0, a full circle is drawn to indicate daily intervals.

Bank, while in the central forecast, it is above Stellwagen Basin and less controlled by topography (see u in Fig. 9 and $\hat{u}$ tendency in Fig. 9b). Another related property is that eigenvectors can extract dominant physical relationships. For example, the tendencies of Fig. 8b contain processes that are not related to pycnocline motions above North Passage (e.g. see $\hat{u}$ and $\hat{v}$ tendencies in Fig. 8b); however, the first vector has eliminated most of them (e.g. see Fig. 7b). Similar remarks can be made for the second vector: compare for example Fig. 12a,b with Fig. 13b. Finally, note that for different domains or grids, the dominant eigenvectors would differ, in accord with the processes occurring in the chosen domain or grid (resolution, etc.). Choosing these parameters is an important research decision, as in every modeling study. The purpose here was mainly sub-mesoscale to Bay-scale variability and the domain and grids were chosen with that in mind.

6. Conclusions

6.1. Method and summary

A data and dynamics-driven methodology to estimate, decompose, organize and analyze the evolving variability of multiscale physical ocean fields was illustrated in a real-time experiment that occurred in Mass. Bay in late summer and early fall of 1998. The dominant variability covariance was initialized based on the approach of Lermusiaux et al. (2000) and forecast based on an ensemble of Monte-Carlo primitive equation model forecasts. Snapshots and tendencies of physical fields and the trajectories of simulated Lagrangian drifters were used to diagnose, evaluate and study the dominant variability covariance. The Monte-Carlo forecast of the variability subspace provided important clues on the location and dynamical nature (e.g. multivariate and/or 3D, local or global, close to thermal-wind balance or not) of the events estimated. It allowed to select dynamically important tendencies, snapshots and drifters, and so guided the dynamical analysis of the variations of physical fields.

6.2. Variability subspace and Mass. Bay dynamics

For the Sep. 27–Oct. 1 period analyzed in detail, which corresponds to the stratified season in transition to fall conditions, the atmospheric forcings, pressure force and Coriolis force were found to be the main drivers of variability. The 3D variability standard deviation forecasts showed that the temperature and salinity variations can be largest in different regions which is indicative of independent tracer effects. Overall, the dominant tracer deviations were found: (i) in coastal upwelling or downwelling regions, where T and S variations were usually coupled, and (ii) at the location of density-driven gyres, vortices or jets subject to relatively large changes (feature displaced, mixed or replaced), where only one of the T or S variation often dominated in the upper layers. The velocity standard deviations, which suggest the features of dominant changes in kinetic energy, were found largest along (i) frontal zones and (ii) topographic features.

The first eigenvector of the normalized variability covariance forecast indicated a direction in the variability space related to a displacement of the Gulf of Maine coastal current offshore from Cape Ann and the corresponding possible creation of adjacent mesoscale recirculation cells. Its 3D structure was described and used to carry out a more detailed analysis of processes near North Passage. The similarities between the vector and tendencies of the central forecast fields increased with time, in accord with fading-memory variability covariances (Appendix B). The trajectories of simulated drifters confirmed the variations of the coastal inflow at Cape Ann and meandering of the Gulf of Maine coastal current along Stellwagen Bank. The main dynamical factors involved above North Passage were found to be, successively, the reversal of the strong wind forcings and Bay-scale surface pressure (deformation) field, the associated Ekman transports and downwelling/upwelling processes, the Coriolis force and inertia.

The second vector forecast indicated a direction associated with a Bay-wide coastal upwelling mode from Barnstable Harbor to Gloucester, in response to strong southerly winds (e.g. 2.1 dyn/cm^2). The 3D structures of the upwelling were captured. For example, deep waters were exposed in surface at the coast and vigorously advected offshore, the width of the upwelling narrowed as depth increased, and amplitudes were maximum near the pycnocline. Two interesting properties of this vector were its barotropic component which showed a Bay-wide anticyclonic vertically averaged circulation, and its vertical cross-Bay structures which showed an offshore downwelling pattern above Stellwagen Basin. The second vector was again used as a dynamical guide, this time to study details of the Bay-wide upwelling/downwelling regime. The similarities between the variations in time of the central forecast fields and cross-sections in the vector confirmed the possibility of cross-Bay vertical cells. Trajectories of simulated drifters illustrated a few 3D properties of the coastal upwelling flows.

Of course, even though major events were indicated by the first two vectors, several other events were related to lower vectors, e.g. displacement of the coastal current outflow at Race Point, upwelling/downwelling in Cape Cod Bay, see Section 5.2.3. In general, the eigendecomposition looks for patterns which explain the maximum volume variations of normalized kinetic and potential energies. It selects here patterns related to variations of the pycnocline and buoyancy flow around Oct. 1. In the surface Ekman mixing-layer, the Bay-wide kinetic effects of the winds have a limited potential energy signature; they are thus represented by vectors of lower eigenvalues. These vectors were not discussed because a rigorous analysis of the physical meaning of the complete variability subspace usually requires additional machinery, in part because of the orthogonality constraint. As we have found elsewhere (Lermusiaux, 1999a,b; Lermusiaux et al., 2000), in certain cases, some vectors may be directly physically meaningful (usually the first ones), while in other cases, vectors should be appropriately grouped to describe a (coherent) structure or a phenomena.

In either case, evolving the variability subspace locates the field variations of largest variance. This property was helpful here to identify a few dynamical characteristics of the data-driven physical field simulation. Strong wind events (wind stress >1 dyn/cm^2) were found to alter the structures of the buoyancy flow. Because of the coastline geometry (Fig. 1), regardless of the wind direction, sufficiently strong winds led to both upwelling and downwelling somewhere in the Bay. Winds in the along-bay direction favored Bay-wide responses. For the two strong wind events estimated, northerly winds could amplify the Bay-wide cyclonic circulation and coastal jet, in accord with observations of Geyer et al. (1992), while southerly winds could destroy these, creating a tendency towards Bay-wide anticyclonic motions. In particular, downwelling and possible strengthening of the cyclonic rim current by coastal frontogenesis were found important. The field variations selected based on the two vectors suggested that the local accelerating or decelerating character of these along-front rim currents was usually associated with a modulation and possible reversal of the ageostrophic vertical velocity patterns in sections across the coastal front. The circulation features were also found to be more variable than previously described. During the 4 days described in detail, several gyres, vortices and currents were estimated to occur, including: a pair of anticyclonic gyres, one in Cape Cod Bay and the other north of Cape Cod Bay; a cyclonic or anticyclonic gyre in northern Mass. Bay; two of the branches of the Gulf of Maine coastal current, one meandering along Stellwagen Bank without entering Mass. Bay and the other entering the Bay but not Cape Cod Bay; a recirculation vortex along Cape Ann, north of the Gulf of Maine coastal current inflow; and upwelling-induced, northward rim currents inside Mass. Bay.

6.3. Variability subspace and a few research directions

The oceanic issues related to the computation of averages were discussed in the text and Appendix B. For dynamical interpretations, they appear especially important when the time-averaged properties are allowed to evolve dynamically on multiple scales, or when the ensemble-averaged statistics is computed based on dynamical equations that are deterministic in nature or already scale-restricted. The present approach, rooted in evolving dominant eigendecompositions, provides a framework to address some of these issues, especially when systems are large and complex like the ocean.

The data and dynamics-driven forecast of the evolving variability subspace is connected to other research areas. It extends the use of fixed "proper orthogonal decompositions" to extract coherent structures in turbulent flows (Lumley, 1981; Sirovich, 1991; Holmes et al., 1998). It is related to the dominant subspace of the so-called GFD singular vectors (Palmer et al., 1998). Since variability is intimately linked with uncertainty and predictability, it is also motivated by probability or error predictions (Ehrendorfer, 1997), skill and predictive capability assessments (Thacker and Lewandowicz, 1996; Moore and Kleeman, 1998; Miller and Cornuelle, 1999), data assimilation (Verlaan and Heemink, 1997; Houtekamer and Mitchell, 1998; Robinson et al., 1998; Brasseur et al., 1999; Madsen and Canizares, 1999; Miller et al., 1999; Voorrips et al., 1999) and adaptive sampling designs, as was shown here and in other regions (Lermusiaux, 1997, 1999b).

Acknowledgements

All members of the LOOPS and AFMIS-CMAST programs are thanked for their helpful collaboration. I am grateful to Prof. D.G.M. Anderson, Dr. J. Dusenberry and Dr. C.J. Lozano for their constructive comments on the manuscript. The experience of Dr. P.J. Haley, Dr. C.J. Lozano and Prof. A.R. Robinson were valuable for using the Harvard Ocean Prediction System. I thank individuals and crew members who helped collecting the MBST-98 data, the MWRA for historical data, and Mr. W.G. Leslie for the data management. I am grateful to Dr. R. Signell, Dr. D.V. Kroujiline and Prof. A. Gangopadhyay for background discussions, and to Ms. M. Armstrong for preparing some of the figures. I am thankful to three anonymous referees for their helpful reviews. The US-National Ocean Partnership Program and Office of Naval Research are thanked for their support under grants ONR-N00014-97-1-1018 to Harvard University. The Fleet Numerical Meteorologic and Oceanographic Center provided the atmospheric data.

Appendix A. Evolving the variability subspace: mathematical problem statement

Choosing the framework of continuous-discrete estimation (Jazwinski, 1970), the measurements are assumed discrete in time. The dynamical equations for the ocean state are considered in their discretized form in space. The notation of Ide et al. (1997) is followed, except for a few shorthands.[6] The state

[6] Denoting space and time by (r,t), the shorthands $\boldsymbol{x}$, $\mathscr{M}(\boldsymbol{x})$ and $\mathrm{d}\eta$ are employed in Eq. (A1a) instead of $\boldsymbol{x}(r,t)$, $\mathscr{M}(\boldsymbol{x}(r,t),r,t)$ and $\mathrm{d}\eta(r,t)$. Similar statements apply to quantities in Eqs. (A1b)–(5) and in Appendix B. Initial conditions are distinguished by a t_0 dependence, e.g. $\boldsymbol{x}(t_0)$. The superscript $(\cdot)^{\mathrm{t}}$ for "true" is omitted, e.g. $\boldsymbol{x}$ and $\mathrm{d}\eta$ are used for $\boldsymbol{x}^{\mathrm{t}}$ and $\mathrm{d}\eta^{\mathrm{t}}$.

vector $\boldsymbol{x} \in \mathbf{R}^n$ is characterized by the stochastic dynamical and measurement models, respectively,

$$\mathrm{d}\mathbf{x} = \mathscr{M}(\mathbf{x})\mathrm{d}t + \mathrm{d}\eta, \tag{A1a}$$

$$\mathbf{y}^{\mathrm{o}} = \mathscr{H}(\mathbf{x}) + \epsilon. \tag{A1b}$$

In Eq. (A1a), $\mathscr{M}$ is the dynamics operator, η a stochastic forcing (Wiener process or Brownian motion, e.g. Gard, 1988; Ikeda and Watanabe, 1989; Holden et al., 1996) of zero mean and covariance matrix $\mathbf{Q} \doteq \varepsilon\{\mathrm{d}\eta\mathrm{d}\eta^{\mathrm{T}}\}/\mathrm{d}t$ (for noise properties and finite-difference implementation, see Lermusiaux, 1997). In Eq. (A1b), $\boldsymbol{y}^{\mathrm{o}} \in \mathbf{R}^m$ is the observation vector, $\mathscr{H}$ the observation operator and ϵ a stochastic forcing of zero mean and covariance matrix $\mathbf{R} \doteq \boldsymbol{\varepsilon}\{\epsilon\epsilon^{\mathrm{T}}\}$, where $\boldsymbol{\varepsilon}\{\cdot\}$ is the expectation operator and $(\cdot)^{\mathrm{T}}$ denotes transposition. The "central forecast" is a solution of Eq. (A1a), or sample path realization, with initial condition $\boldsymbol{x}(t_0)$. The expected evolution of the ocean state is obtained by taking the expectation of Eq. (A1a),

$$\frac{\mathrm{d}\boldsymbol{\varepsilon}\{\mathbf{x}\}}{\mathrm{d}t} = \boldsymbol{\varepsilon}\{\mathscr{M}(\mathbf{x})\}, \tag{A2}$$

the initial condition being $\boldsymbol{\varepsilon}\{\boldsymbol{x}\}(t_0)$. The evolution equation of the variability covariance from the expected state of Eq. (A2),

$$\mathbf{P} \doteq \boldsymbol{\varepsilon}\left\{(\mathbf{x} - \boldsymbol{\varepsilon}\{\mathbf{x}\})(\mathbf{x} - \boldsymbol{\varepsilon}\{\mathbf{x}\})^{\mathrm{T}}\right\} \in \mathbf{R}^{n\times n}, \tag{A3}$$

is obtained by first forming the time-rate-of-change of $(\boldsymbol{x} - \boldsymbol{\varepsilon}\{\boldsymbol{x}\})(\boldsymbol{x} - \boldsymbol{\varepsilon}\{\boldsymbol{x}\})^{\mathrm{T}}$ using the Itô lemma or rule for Wiener processes (Jazwinski, 1970), and Eqs. (A1a) and (A2) to replace $\mathrm{d}\boldsymbol{x}$ and $\mathrm{d}\boldsymbol{\varepsilon}\{\boldsymbol{x}\}$. Taking the expectation of the result then leads to,

$$\frac{\mathrm{d}\mathbf{P}}{\mathrm{d}t} = \boldsymbol{\varepsilon}\left\{(\mathbf{x} - \hat{\mathbf{x}})\left(\mathscr{M}(\mathbf{x}) - \hat{\mathscr{M}}(\mathbf{x})\right)^{\mathrm{T}}\right\} + \boldsymbol{\varepsilon}\left\{\left(\mathscr{M}(\mathbf{x}) - \hat{\mathscr{M}}(\mathbf{x})\right)(\mathbf{x} - \hat{\mathbf{x}})^{\mathrm{T}}\right\} + \mathbf{Q}, \tag{A4a}$$

$$\frac{\mathrm{d}\mathbf{P}}{\mathrm{d}t} = \boldsymbol{\varepsilon}\{\mathbf{x}\mathscr{M}^{\mathrm{T}}(\mathbf{x})\} - \hat{\mathbf{x}}\hat{\mathscr{M}}^{\mathrm{T}}(\mathbf{x}) + \boldsymbol{\varepsilon}\{\mathscr{M}(\mathbf{x})\mathbf{x}^{\mathrm{T}}\} - \hat{\mathscr{M}}(\mathbf{x})\hat{\mathbf{x}}^{\mathrm{T}} + \mathbf{Q}, \tag{A4b}$$

where $\hat{\boldsymbol{x}} \doteq \varepsilon\{\boldsymbol{x}\}$ and $\hat{\mathscr{M}}(\boldsymbol{x}) \doteq \varepsilon\{\mathscr{M}(\boldsymbol{x})\}$ have been used to lighten the notation.

The present objective is to initialize and evolve the "dominant" eigendecomposition of $\mathbf{P}$, combining data and dynamics. By "dominant" is meant the components explaining most of the variance, i.e. the largest or significant p eigenvalues and corresponding eigenvectors of $\mathbf{P}$. An estimate of this dominant, rank-p eigendecomposition is denoted by,[7]

$$\mathbf{B}^p \doteq \mathbf{E}\,\Pi\,\mathbf{E}^{\mathrm{T}}, \tag{A5}$$

where the diagonal of Π and columns of $\boldsymbol{E}$ contain the ordered p eigenvalue and eigenvector estimates. Hence, the goal is to compute $\mathbf{B}^p(t_0) \doteq \boldsymbol{E}_0\,\Pi_0\,\boldsymbol{E}_0^{\mathrm{T}}$ and evolve it, i.e. compute $\mathbf{B}^p(t) \doteq \boldsymbol{E}_t\,\Pi_t\,\boldsymbol{E}_t^{\mathrm{T}}$ based on Eqs. (A1a)–(4b); a methodology to do so is outlined in Section 4. In Eqs. (A4a,b), the nonlinear and stochastic terms continuously excite new directions in the state space. An adequate rank p (e.g. such that the trace of $\mathbf{P}(t) - \mathbf{B}^p(t)$ is small enough) is thus function of time, $p = p(t)$; the notation p is only used for convenience. Note that Eqs. (A4a,b) also govern the predictability error covariance from the expected state. It is the initial conditions and reference state which determine the difference between predictability error and variability covariances.

Appendix B. Classic empirical orthogonal functions, covariance eigendecomposition and variability subspaces

A few relationships and issues concerning the eigendecompositions of time-averaged sample covariances (spatial EOFs) and of dynamically evolving covariances (Eqs (A4a)–(5)) are discussed. The classic time-averaged sample covariance is first extended to fading-memory sample covariances so as to obtain a differential equation and allow some direct comparisons with Eqs. (A4a)–(5). A few properties are then discussed and links to constant subspace techniques, for example used in turbulence studies (Holmes et al., 1998), are mentioned.

[7] All decompositions are carried out on non-dimensionalized covariances so as to be unit independent. For sample covariances (Section 4), the norm used for each field variation is the volume and sample averaged variance, as in Lermusiaux and Robinson (1999). Once the non-dimensional sample covariance matrix is decomposed, the non-dimensional eigenvectors, denoted here by $\boldsymbol{E}^*$, are renormalized to lead $\boldsymbol{E}$ in Eq. (A5).

B.1. Conventional sample covariances and spatial EOFs

Generally, the computation of spatial EOFs involves time-averaging. For simplicity, it is assumed here that full fields are measured, i.e. Eq. (A1b) reduces to $\boldsymbol{y}^{\mathrm{o}} = \boldsymbol{x} + \boldsymbol{\epsilon}$, and that N observations $\boldsymbol{y}_i^{\mathrm{o}} = \boldsymbol{x}(t_i) + \boldsymbol{\epsilon}_i$, $i = 1,\ldots,N$, are made at intervals Δt over a period $\tau = N\Delta t$. Removing the time average of these observations, $\bar{\mathbf{y}}^{\mathrm{o}} \doteq 1/N\sum_{i=1}^{N}\boldsymbol{y}_i^{\mathrm{o}} = \bar{\mathbf{x}} + \bar{\boldsymbol{\epsilon}}$, the spatial EOFs are the eigenvectors of the sample covariance matrix,

$$\mathbf{C}_s \doteq \frac{1}{N}\sum_{i=1}^{N}\left(\tilde{\mathbf{y}}_i^{\mathrm{o}}\tilde{\mathbf{y}}_i^{\mathrm{o}\mathrm{T}} - \tilde{\boldsymbol{\epsilon}}_i\tilde{\boldsymbol{\epsilon}}_i^{\mathrm{T}}\right)$$

$$= \frac{1}{\tau}\sum_{i=1}^{N}\left(\tilde{\mathbf{y}}_i^{\mathrm{o}}\tilde{\mathbf{y}}_i^{\mathrm{o}\mathrm{T}} - \tilde{\boldsymbol{\epsilon}}_i\tilde{\boldsymbol{\epsilon}}_i^{\mathrm{T}}\right)\Delta t, \qquad \text{(B1)}$$

where $\tilde{\boldsymbol{y}}_i^{\mathrm{o}} \doteq \tilde{\boldsymbol{y}}_i^{\mathrm{o}} - \bar{\boldsymbol{y}}^{\mathrm{o}}$, $\tilde{\boldsymbol{\epsilon}}_i \doteq \boldsymbol{\epsilon}_i - \bar{\boldsymbol{\epsilon}}$, and $\sum_{i=1}^{N}\tilde{\mathbf{y}}_i^{\mathrm{o}}\,\tilde{\boldsymbol{\epsilon}}_i^{\mathrm{T}}/N$ which $\rightarrow 0$ as $N \rightarrow \infty$ is neglected. For Δt approaching zero holding τ, the continuous version $\mathbf{C}$ of $\mathbf{C}_s$ in Eq. (B1) is,

$$\mathbf{C} \doteq \frac{1}{\tau}\int_{t-\tau}^{t}\tilde{\mathbf{x}}\tilde{\mathbf{x}}^{\mathrm{T}}d\sigma, \qquad \text{(B2)}$$

where the $(\tilde{\boldsymbol{y}}_i^{\mathrm{o}} - \tilde{\boldsymbol{\epsilon}}_i)$'s are replaced by their limit, $\tilde{\boldsymbol{x}} \doteq \tilde{\boldsymbol{y}}^{\mathrm{o}} - \tilde{\boldsymbol{\epsilon}} \doteq \boldsymbol{x} - \bar{\boldsymbol{x}}$, with $\bar{\mathbf{x}} \doteq 1/\tau\int_{t-\tau}^{t}\mathbf{x}\mathrm{d}\sigma$.

There are a few ambiguities related to Eqs. (B1) and (B2). As stated, the conventional EOFs are constant for the time window of interest. However, for different windows $[t-\tau, t]$, the time average $\bar{\boldsymbol{y}}^{\mathrm{o}}$ as well as $\mathbf{C}_s$ and its EOFs in Eq. (B1) usually change. In computing Eq. (B2), one thus implicitly expects that $\mathbf{C}$ and its eigendecomposition can vary in time, but on time-scales longer than $\mathscr{O}(\tau)$. For such non-stationary signals, another issue is the determination of meaningful sizes for τ (e.g. Phillips et al., 1992); for the multiple variables, scales and processes, common sense is still often the only guide, especially in oceanography. If $\boldsymbol{x}$ in and Eqs. (B1) and (B2) is a model state, since Eq. (A1a) is already scale-restricted, τ should be compatible with the spectral window of Eq. (A1a), e.g. Nihoul (1993). The choice of τ is thus a research question. The time to which $\mathbf{C}$ in Eq. (B2) corresponds is finally somewhat arbitrary. In practice, one computes the variability once data are available and definition (B2) is here understood as that of $\mathbf{C}(t)$, i.e. the value at the end of the time interval. This is a common choice in dynamical system theory (e.g. Dehaene, 1995, and references therein), but the discussion to follow holds for other choices.

B.2. Fading-memory sample covariances and spatial EOFs

For a comparison between $\mathbf{P}$ in Eqs. (A4a,b) and $\mathbf{C}$, definition (B2) should be extended to a matrix whose evolution is continuous and governed by an ordinary differential equation.

The rectangular filter of width τ used to select $\mathbf{C}$ should be replaced. A useful property is that most oceanic systems Eq. (A1a) are dissipative and have limits of predictability: the memory of initial conditions often fades away with time. Explicitly using this, the weights of older $\tilde{\boldsymbol{x}}$ in Eq. (B2) can be reduced according to a forgetting or fading rate λ. This rate λ can adapt to the evolving statistical properties of $\tilde{\boldsymbol{x}}$. With a first two moments approach (Section 2), λ then varies with the state, the variability covariance itself and time. From these arguments, a class of so-called fading-memory sample covariances (e.g. Brockett, 1990) is introduced,

$$\mathbf{C}_\lambda(t) \doteq \frac{1}{\mu}\int_{-\infty}^{t}\tilde{\mathbf{x}}(\sigma)\tilde{\mathbf{x}}^{\mathrm{T}}(\sigma)\mathrm{e}^{-\int_\sigma^t\lambda(\mathbf{C}_\lambda(\eta),\tilde{\mathbf{x}}(\eta),\eta)\mathrm{d}\eta}\mathrm{d}\sigma. \qquad \text{(B3)}$$

In Eq. (B3), μ is a normalization factor, λ a positive functional and $\tilde{\boldsymbol{x}}$ is the variation $\boldsymbol{x} - \bar{\boldsymbol{x}}$, where the average of Appendix B.1 is extended to the evolving average $\bar{\mathbf{x}} \doteq 1/\mu\int_{-\infty}^{t}\mathbf{x}\mathrm{e}^{-\int_\sigma^t\lambda\mathrm{d}\eta}\mathrm{d}\sigma$ for consistency. The matrix $\mathbf{C}_\lambda$ can be understood as a sample estimate of $\mathbf{P}$ in Eqs. (A3–4b if μ is set to the integral of the kernel for Eq. (B3), i.e.,

$$\mu(t) \doteq \int_{-\infty}^{t}\mathrm{e}^{-\int_\sigma^t\lambda(\mathbf{C}_\lambda(\eta),\tilde{\mathbf{x}}(\eta),\eta)\mathrm{d}\eta}\mathrm{d}\sigma. \qquad \text{(B4)}$$

Note that if only EOFs are sought, μ is not a relevant scalar. The rate $\lambda > 0$ is required for $\mathbf{C}_\lambda(t)$ to be defined: if the variations $\tilde{\boldsymbol{x}}(\sigma)$ over $[-\infty, t]$ are finite, $\mathbf{C}_\lambda(t)$ stays bounded as time increases. Definitions (B3) and (B4) include several of the previously introduced fading-memory schemes: for example, $\lambda = \mathrm{cst}$ (Dehaene, 1995), $\lambda = \tilde{\boldsymbol{x}}^{\mathrm{T}}\mathbf{C}_{\lambda}\tilde{\boldsymbol{x}}$ (Brockett, 1990) or λ evolving with the error estimate of $\tilde{\boldsymbol{x}}$ (Haykin, 1996). The direct extension of Eq. (B2) corresponds to $\lambda = 1/\tau$. In that case, evaluating Eq. (B4) gives a constant, $\mu = \tau$, and Eq. (B3) becomes,

$$\mathbf{C}_{1/\tau}(t) \doteq \frac{1}{\tau}\int_{-\infty}^{t}\tilde{\mathbf{x}}(\sigma)\tilde{\mathbf{x}}^{\mathrm{T}}(\sigma)\mathrm{e}^{-\frac{(t-\sigma)}{\tau}}\mathrm{d}\sigma, \quad \text{(B5)}$$

which is a fading-memory sample covariance of decay time-scale τ. For oceanic studies, using λ as a function of $\mathbf{C}_{\lambda}$ and $\tilde{\boldsymbol{x}}$ allows past variability estimates and events to be "remembered" at time t with different weights. Ideally, λ can be a matrix so as to account for inhomogeneous and anisotropic effects.

With the extension Eqs. (B3) and (B5) of Eq. (B2), rates-of-change that only depend on the values of fields at time t can be computed. An ordinary differential equation can then be derived and comparisons made with Eqs. (A4a,b). Using the Leibnitz theorem, one obtains from Eq. (B3),

$$\frac{\mathrm{d}\mathbf{C}_{\lambda}}{\mathrm{d}t} = \frac{\tilde{\mathbf{x}}\tilde{\mathbf{x}}^{\mathrm{T}}}{\mu} - \frac{\mathbf{C}_{\lambda}}{\mu}, \quad \text{(B6)}$$

where $(\mathrm{d}\mu)/(\mathrm{d}t) = 1 - \lambda\mu$ has been used. In particular, for $\lambda = 1/\tau$ (Eq. (B5)), $(\mathrm{d}\mathbf{C}_{1/\tau})/(\mathrm{d}t) = (\tilde{\boldsymbol{x}}\tilde{\boldsymbol{x}}^{\mathrm{T}})/(\tau) - (\mathbf{C}_{1/\tau})/(\tau)$. The RHS of Eq. (B6) is a simplified model of Eqs. (A4a,b): the first term is a weighted influence of the most recent field variations due to both dynamical ($\mathscr{M}$) and stochastic ($\mathbf{Q}$) effects, while the second corresponds to the components of the dynamics ($\mathscr{M}$) that are variance-decreasing. Another relation with Eqs. (A4a,b) is obtained for the case $\mu = \tau$ (in general $\mu = \mathrm{cst}$) by directly taking the expectation of Eq. (B5). Since the integral and expectation operator commute,

$$\boldsymbol{\varepsilon}\{\mathbf{C}_{1/\tau}\}(t) = \frac{1}{\tau}\int_{-\infty}^{t}\boldsymbol{\varepsilon}\{\tilde{\mathbf{x}}(\sigma)\tilde{\mathbf{x}}^{\mathrm{T}}(\sigma)\}\mathrm{e}^{-\frac{(t-\sigma)}{\tau}}\mathrm{d}\sigma. \quad \text{(B7)}$$

This logically states that the expectation of $\mathbf{C}_{1/\tau}$ is equal to the time average of $\boldsymbol{\varepsilon}\{\tilde{\boldsymbol{x}}\tilde{\boldsymbol{x}}^{\mathrm{T}}\}$. This is not sufficient however for the expectation of $\mathbf{C}_{1/\tau}$ to be the time average of $\mathbf{P}$. The matrix $\boldsymbol{\varepsilon}\{\tilde{\boldsymbol{x}}\tilde{\boldsymbol{x}}^{\mathrm{T}}\}$ is only a good approximation of $\mathbf{P}$ if $\bar{\mathbf{x}}(t) = 1/\tau\int_{-\infty}^{t}\mathbf{x}\mathrm{e}^{-\frac{(t-\sigma)}{\tau}}\mathrm{d}\sigma$ is a good estimate of $\boldsymbol{\varepsilon}\{\boldsymbol{x}\}(t)$. Hence, for $\mathbf{C}_{1/\tau}$ and $\mathbf{P}$ to be equal, the expectation and time average must have equivalent effects on the first two moments of $\boldsymbol{x}$, which is an ergodic hypothesis.

B.3. Discussion

In the present scheme and examples (Sections 3–5), it is the evolving dominant eigendecomposition of $\mathbf{P}$ in Eqs. (A4a,b), i.e. $\mathbf{B}^{p}$ in Eq. (A5), which is estimated and forecasted. Hence, the approach is to decompose the variability computed based on ensemble averaging, at a given fixed time.

In turbulence studies, the use of ensemble averaging over many identical experiments (Eqs. (A2–5)), instead of time-averaging of a single experiment (Eqs. (B1–7)) is usually advocated for experimental, theoretical or mathematical reasons (e.g. Salmon, 1998; von Storch and Frankignoul, 1998; Nihoul and Beckers, 1999). This point of view is usually shared by some statisticians or stochastic modelers. Despite these facts, there are some ambiguities related to Eqs. (A2–5, as there were ambiguities related to Eqs. (B1–7 (see Appendices B.1 and B.2). First, the present ensemble averaging is not carried out on the true fields, but on the already averaged or scale-restricted state variables and approximate dynamics (A1a,b). This issue may not be too important as long as closure terms in Eqs. (A1a,b) are proper or limited in amplitude. Computing ensemble averages based on Eqs. (A1a,b) is in fact what is commonly carried out in practice (e.g. Holmes et al., 1998; von Storch and Frankignoul, 1998, and references therein). Using both real data and dynamics as done here (Sections 3–5) also helps in addressing this concern. Second, the dynamical interpretation of ensemble averages for ocean dynamics is not immediate. Such an average at time t (Eqs. (A2–5)) combines the effects of all oceanic events that occurred before t and it is challenging to discriminate between these effects. Third and perhaps more importantly, there is a priori no variability in the true ocean at a fixed time t: there is only one single ocean state. From this point of view, usually shared by some dynamicists or deterministic modelers, the expectation operator and thus all ensemble properties somewhat lack of meaning. Probability ideas mainly arise because our approximate knowledge (Eqs. (A1a,b)), while time-averaging can be carried out in Eqs. (B2–7 without any implicit stochastic assumptions on $\tilde{\boldsymbol{x}}$.

The extension of the time-averaged covariances to fading-memory covariances provides a framework to compare ensemble-averaged (probabilistic) and time-averaged definitions of evolving variability covariances (Appendix B.2). It should be useful to address some of the above issues. In the present Mass. Bay example, simple links to time-variations of the estimated fields were already found valuable to evaluate and improve the dynamical interpretation of ensemble-averaged covariances (Section 5). Since the present covariances are allowed to evolve, tracking their dominant eigendecompositions also provides an extension to the already useful fixed subspace approaches, like the "proper orthogonal decomposition" (Lumley, 1971, 1981), Karhunen–Loéve procedure (Sirovich, 1991; Rajaee et al., 1994) or classic EOF expansion (Eqs. (B1) and (B2)). The present variability subspace evolves in time, exploring the neighborhood of $\boldsymbol{\varepsilon}\{\boldsymbol{x}\}(t)$, and it is estimated combining data and dynamics. It aims to follow the dominant coherent structures as they develop, interact or subside, and may help find a few answers to some turbulence and ocean dynamics questions.

Appendix C. Timings of the real-time computations

The initialization of the physical fields for Sep. 27 (Section 5.1.1) took about 30 min late on Sep. 27. The initialization of the 3D physical variability subspace (Section 5.1.2) was completed on Sep. 28, in a total of 15.5 h. To do so, the dominant 300 tracer eigenvectors were first computed in about 1 h. The complete variability subspace for 300 PE eigenvectors was then constructed in 14.5 h: using an average computer power equivalent to 16 Sun Sparc-20 CPUs, the ensemble of 300 adjustment PE integrations took $(300/16 \times 40)/60 = 12.5$ h, and the SVDs and associated evaluations of the convergence criterion (Lermusiaux, 1997) took about 2 h. Each of the 300 adjustments were for 1 model-day, taking about 40 min on a Sun Sparc-20 (this time could have been reduced by increasing the time-step).

Using Eq. (A1a), the 4-day "central forecast" for Oct. 1 (Section 5.2.1) was issued mid-day on Sep. 28, in about 100 min with a Sun Ultra. The 4-day Monte-Carlo forecasts (Sections 5.2.2 and 5.2.3) were started on Sep. 28 and completed in about 2.5 days of elapsed-time, late on Sep. 30: using an average computer power equivalent to 17 Sun Sparc-20 CPUs, the ensemble of 296 Monte-Carlo 4-day forecasts required $296/17 \times 200/60/24 = 2.42$ days, and the SVDs and convergence criterion computations took an additional 1.5 h. Late on Sep. 29, the 136 forecasts already available were used in the design of the sampling for Sep. 30 (Section 5.2.2).

References

Anderson, D.M., 1997. Bloom dynamics of toxic Alexandrium species in the northeastern US. Limnol. Oceanogr. 42, 1009–1022.

Atlas, R., 1997. Atmospheric observations and experiments to assess their usefulness in data assimilation. J. Meteorol. Soc. Jpn. 75 (1B), 111–130.

Bennett, A.F., 1992. Inverse methods in physical oceanography. Cambridge Monographs on Mechanics and Applied Mathematics. Cambridge Univ. Press.

Blumberg, A.R., Signell, R.P., Jenter, H., 1993. Modeling transport processes in the coastal ocean. J. Environ. Eng. 1, 31–52.

Bogden, P.S., Malanotte-Rizzoli, P., Signell, R.P., 1996. Open-ocean boundary conditions from interior data: local and remote forcing of Massachusetts Bay. J. Geophys. Res. 101 (C3), 6487–6500.

Brasseur, P., Ballabrera-Poy, J., Verron, J., 1999. Assimilation of altimetric data in the mid-latitude oceans using the Singular Evolutive Extended Kalman filter with an eddy-resolving, primitive equation model. J. Mar. Syst. 22 (4), 269–294.

Brockett, R.W., 1990. Dynamical systems that learn subspaces. Mathematical Systems Theory: The Influence of R.E. Kalman. Springer-Verlag, pp. 410–420.

Brown, W.S., 1998. Wind-forced pressure response of the Gulf of Maine. J. Geophys. Res. 103 (C13), 30661–30678.

Candela, J., Lozano, C.J., 1995. Barotropic response of the Western Mediterranean to observed atmospheric pressure forcing. In: La Violette, P.E. (Ed.), Coastal and Estuarine Studies: Seasonal and Interannual Variability of the Western Mediterranean Sea, pp. 325–359.

Chen, M.-H., Shao, Q.-M., Ibrahim, J.G., 2000. Monte Carlo Methods in Bayesian Computation. Springer Series in Statistics, Springer.

Chereskin, T.K., 1983. Generation of internal waves in Massachusetts Bay. J. Geophys. Res. 88 (C4), 2649–2661.

Csanady, G.T., 1977. Intermittent 'full' upwelling in Lake Ontario. J. Geophys. Res. 82, 397–419.

Cushman-Roisin, B., 1994. Introduction to Physical Oceanography. Prentice-Hall.

Curtin, T.B., Bellingham, J.B., Catipovic, J., Webb, D., 1993.

Autonomous ocean sampling networks. Oceanography 6 (3), 86–94.

Daley, R., 1991. Atmospheric Data Analysis. Cambridge Univ. Press.

Dehaene, J., 1995. Continuous-Time Matrix Algorithms Systolic Algorithms and Adaptive Neural Networks. Department Elektrotechniek-Esat, Faculteit Toegepaste Wetenschappen, Katholieke Universiteit Leuven, Leuven (Heverlee), 233 pp.

Ehrendorfer, M., 1997. Predicting the uncertainty of numerical weather forecasts: a review. Meteorol. Z. 6 (4), 147–183.

Evensen, G., 1994. Inverse methods and data assimilation in nonlinear ocean models. Physica D 77, 108–129.

Gard, T.C., 1988. Introduction to stochastic differential equations. Monographs and Textbooks in Pure and Applied Mathematics. Dekker.

Garwood Jr., R.W., Gallacher, P.C., Muller, P., 1985. Wind direction and equilibrium mixed layer depth: general theory. J. Phys. Oceanogr. 15, 1325–1331.

Geyer, W.R., Ledwell, J.R., 1997. Boundary mixing in Massachusetts Bay. MWRA Enviro. Quality Dept. Tech. Rpt. Series No 97–9. Massachusetts Water Resources Authority, Boston, MA, 20 pp.

Geyer, W.R., Gardner, G.B., Brown, W.S., Irish, J., Dutman, B., Loder, T., Signell, R.P., 1992. Physical oceanographic investigation of Massachusetts and Cape Cod Bays, Report to the Massachusetts Bays Program MBP-92-03, 497 pp.

Gerkema, T., 1996. A unified model for the generation and fission of internal tides in a rotating ocean. J. Mar. Res. 54, 421–450.

Ghil, M., Malanotte-Rizzoli, P., 1991. Data assimilation in meteorology and oceanography. Adv. Geophys. 33, 141–266, Academic Press.

Graham, A., 1981. Kronecker Products and Matrix Calculus: With Applications. Halsted Press.

Grimshaw, R.H.J., Ostrovsky, L.A., Shrira, V.I., Stepanyants, Y.A., 1998. Long nonlinear surface and internal gravity waves in a rotating ocean. Surv. Geophys. 19, 289–338.

Hackert, E.C., Miller, R.N., Busalacchi, A.J., 1998. An optimized design for a moored instrument array in the tropical Atlantic Ocean. J. Geophys. Res. 103 (C4), 7491–7509.

Halpern, D., 1971. Observations on short-period internal waves in Mass. Bay. J. Mar. Res. 41, 116–132.

Haury, L.R., Briscoe, M.G., Orr, M.H., 1979. Tidally generated internal wave packets in Massachusetts Bay. Nature 278 (5702), 312–317.

Haykin, S.S., 1996. Adaptive Filter Theory. 3rd edn. Prentice Hall, 989 pp.

Hibiya, T., 1988. The generation of internal waves by tidal flow over Stellwagen Bank. J. Geophys. Res. 93 (C1), 533–542.

Holden, H., Oksendal, B., Uboe, J., Zhang, T., 1996. Stochastic partial differential equations. Probability and Its Applications. Birkhäuser.

Holmes, P., Lumley, J.L., Berkooz, G., 1998. Turbulence, Coherent Structures, Dynamical Systems and Symmetry. Cambridge Monographs on Mechanics,, First paperback edition, 420 pp.

Hoskins, B.J., Bretherton, F.P., 1972. Atmospheric frontogenesis models: mathematical formulation and solution. J. Atmos. Sci. 29, 11–37.

Houtekamer, P.L., Derome, J., 1995. Methods for ensemble prediction. Mon. Weather Rev. 123 (7), 2181–2196.

Houtekamer, P.L., Mitchell, H.L., 1998. Data assimilation using an ensemble Kalman filter technique. Mon. Weather Rev. 126 (3), 796–811.

Ide, K., Courtier, P., Ghil, M., Lorenc, A.C., 1997. Unified notation for data assimilation: operational, sequential and variational. J. Meteorol. Soc. Jpn. 75 (1B), 181–189.

Ikeda, N., Watanabe, S., 1989. Stochastic Differential Equations and Diffusion Processes. 2nd edn. North-Holland Mathematical Library, North-Holland.

Jazwinski, A.H., 1970. Stochastic Processes and Filtering Theory. Academic Press.

Kangas, R.E., Hufford, G.L., 1974. An upwelling rate for Massachusetts Bay. J. Geophys. Res. 79 (15), 2231–2236.

Kelly, J.R., 1997. Nitrogen flow and the interaction of Boston Harbor with Mass. Bay. Estuaries 20, 365–380.

Kelly, J.R., 1998. Quantification and potential role of ocean nutrient loading to Boston Harbor. Mar. Ecol.: Prog. Ser. 173, 53–65.

Kelly, J.R., Doering, P.H., 1997. Monitoring and modeling primary production in coastal waters: studies in Massachusetts Bay 1992–1994. Mar. Ecol.: Prog. Ser. 148, 155–168.

Kelly, J.R., Doering, P.H., 1999. Seasonal deepening of the pycnocline in a shallow shelf ecosystem and its influence on near-bottom dissolved oxygen. Mar. Ecol.: Prog. Ser. 178, 151–168.

Kundu, P.K., 1990. Fluid Mechanics. Academic Press, 638 pp.

Large, W.G., McWilliams, J.C., Doney, S.C., 1994. Oceanic vertical mixing: a review and a model with a nonlocal boundary layer parametrization. Rev. Geophys. 32 (4), 363–403.

Lee, C.-Y., Beardsley, R.C., 1974. The generation of long nonlinear internal waves in a weakly stratified shear flow. J. Geophys. Res. 79, 453–462.

Lee, D.K., Niiler, P.P., 1998. The inertial chimney: the near-inertial energy drainage from the ocean surface to the deep layer. J. Geophys. Res. 103 (C4), 7579–7591.

Lermusiaux, P.F.J., 1997. Error subspace data assimilation methods for ocean field estimation: theory, validation and applications. PhD Thesis, May 1997, Harvard Univ., Cambridge, MA.

Lermusiaux, P.F.J., 1999a. Data assimilation via error subspace statistical estimation, Part II: Middle Atlantic Bight shelfbreak front simulations and ESSE validation. Mon. Weather Rev. 127 (7), 1408–1432.

Lermusiaux, P.F.J., 1999b. Estimation and study of mesoscale variability in the Strait of Sicily. Dyn. Atmos. Oceans 29, 255–303. Special issue in honor of Professor A.R. Robinson.

Lermusiaux, P.F.J., Robinson, A.R., 1999. Data assimilation via error subspace statistical estimation, Part I: theory and schemes. Mon. Weather Rev. 127 (7), 1385–1407.

Lermusiaux, P.F.J., Anderson, D.G., Lozano, C.J., 2000. On the mapping of multivariate geophysical fields: error and variability subspace estimates. Q. J. R. Meteorol. Soc., April B, 1387–1430.

Lozano, C.J., Haley, P.J., Arango, H.G., Sloan, Q., Robinson, A.R., 1994. Harvard coastal/deep water primitive equation model. Harvard open ocean model reports No. 52, Harvard Univ., Cambridge, MA.

Lozano, C.J., Robinson, A.R., Arango, H.G., Gangopadhyay, A., Sloan, N.Q., Haley, P.J., Leslie, W.G., 1996. An interdisciplinary ocean prediction system: assimilation strategies and structured data models. In: Malanotte-Rizzoli, P. (Ed.), Modern Approaches to Data Assimilation in Oceano Modelling. Elsevier Oceanography Series, Elsevier, The Netherlands.

Lozier, M.S., McCartney, M., Owens, W.B., 1996. The climatology of the North Atlantic. Prog. Oceanogr. 36, 1–44.

Lumley, J.L., 1971. Stochastic Tools in Turbulence. Academic Press, New York.

Lumley, J.L., 1981. Coherent structures in turbulence. In: Meyer, R.E. (Ed.), Transition and Turbulence. Mathematics Research Center Symposia and Advanced Seminar Series, Academic Press, New York.

MacVean, M.K., Woods, J.D., 1980. Redistribution of scalars during upper ocean frontogenesis: a numerical model. Q. J. R. Meteorol. Soc. 106, 293–311.

Madsen, H., Canizares, R., 1999. Comparison of extended and ensemble Kalman filters for data assimilation in coastal area modelling. Int. J. Numer. Methods Fluids 31, 961–981.

Matsuura, T., Hibiya, T., 1990. An experimental and numerical study of the internal wave generation by tide-topography interaction. J. Phys. Oceanogr. 20, 506–521.

Miller, A.J., Cornuelle, B.D., 1999. Forecasts from fits of frontal fluctuations. Dyn. Atmos. Oceans 29, 305–333. Special issue in honor of Professor A.R. Robinson.

Miller, R.N., Carter, E.F., Blue, S.L., 1999. Data assimilation into nonlinear stochastic models. Tellus 51A, 167–194.

Mofjeld, H.O., Lavelle, J.W., 1984. Setting the length scale in a second-order closure model of the unstratified bottom layer. J. Phys. Oceanogr 14, 833–839.

Moore, A.M., Kleeman, R., 1998. Skill assessment for ENSO using ensemble prediction. Q. J. R. Meteorol. Soc. 124 (B), 557–584.

Nihoul, J.C.J., 1993. Applications of mathematical modeling to the marine environment. In: Zanetti, P. (Ed.), Environmental Modeling, I. Computational Mechanics Publications, England, pp. 75–140.

Nihoul, J.C.J., Beckers, J.M., 1999. Marine turbulence revisited. 29th International Liége Colloquium on Ocean Hydrodynamics. J. Mar. Syst. 21 (1–4).

Nihoul, J.C.J., Djenidi, S., 1998. Coupled physical, chemical and biological models. In: Brink, K.H., Robinson, A.R. (Eds.), The Sea: The Global Coastal Ocean I, Processes and Methods, vol. 10, Wiley, New York, NY.

Oja, E., 1992. Principal components, minor components and linear neural networks. Neural Networks 5, 927–935.

Orlanski, I., 1976. A simple boundary condition for unbounded hyperbolic flows. J. Comput. Phys. 41, 251–269.

Pacanowski, R.C., Philander, S.G.H., 1981. Parametrization of vertical mixing in numerical models of tropical oceans. J. Phys. Oceanogr. 11 (11), 1443–1451.

Palmer, T.N., Gelaro, R., Barkmeijer, J., Buizza, R., 1998. Singular vectors, metrics and adaptive observations. J. Atmos. Sci. 55, 633–653.

Phillips, T.J., Gates, W.L., Arpe, K., 1992. The effects of sampling frequency on the climate statistics of the European center for medium-range weather forecasts. J. Geophys. Res. 97 (D18), 20427–20436.

Price, J.F., 1983. Internal wave wake of a moving storm. Part I: Scales, energy budget and observations. J. Phys. Oceanogr. 13 949–965.

Rajaee, M., Karlsson, S.K.F., Sirovich, L., 1994. Low-dimensional description of free-shear-flow coherent structures and their dynamical behaviour. J. Fluid Mech. 63 (258), 1–29.

Robert, C.P., Casella, G., 1999. Monte Carlo Statistical Methods. Springer Texts in Statistics, Springer.

Robinson, A.R., 1996. Physical processes, field estimation and an approach to interdisciplinary ocean modeling. Earth-Sci. Rev. 40, 3–54.

Robinson, A.R., the LOOPS group, 1999. Real-time forecasting of the multidisciplinary coastal ocean with the Littoral Ocean Observing and Predicting System (LOOPS). Third conference on coastal atmospheric and oceanic prediction and processes (3–5 Nov. 1999), New Orleans, LA. Am. Meteorol. Soc., 30–35.

Robinson, A.R., Lermusiaux, P.F.J., Sloan III, N.Q., 1998. Data assimilation. In: Brink, K.H., Robinson, A.R. (Eds.), The Sea: The Global Coastal Ocean I, Processes and Methods, vol. 10, Wiley, New York, NY.

Rossby, C.G., Montgomery, R.G., 1935. The layer of frictional influence in wind and ocean currents. Pap. Phys. Oceanogr. Meteor. 3, Annual Reviews, 101 pp.

Rothschild, B., the AFMIS group, 1999. Advanced fisheries management information system, AFMIS report, NASA NAG13-48.

Salmon, R., 1998. Lectures on Geophysical Fluid Dynamics. Oxford Univ. Press.

Shapiro, R., 1970. Smoothing, filtering and boundary effects. Rev. Geophys. and Space Phys. 8 (2), 359–387.

Signell, R.P., Butman, B., 1992. Modeling tidal exchange and dispersion in Boston Harbor. J. Geophys. Res. 97, 15591–15606.

Signell, R.P., List, J.H., 1997. Effect of wave-enhanced bottom friction on storm-driven circulation in Massachusetts Bay. J. Waterw., Port, Coast. Ocean Eng., ASCE 123 (5), 233–239.

Signell, R.P., Jenter, H.L., Blumberg, A.F., 1993. Modeling the seasonal circulation in Massachusetts Bay. Estuarine and Coastal Modeling III, Proceedings of the 3rd International Conference, Sponsored by Waterway, September, 1993, Oak Brook, IL.

Spall, M.A., 1995. Frontogenesis, subduction and cross-front exchange at upper ocean fronts. J. Geophys. Res. 100, 2543–2557.

Spall, M.A., 1997. Baroclinic jets in confluent flow. J. Phys. Oceanogr. 27, 1054–1071.

Sirovich, L., 1991. Analysis of turbulent flows by means of the empirical eigenfunctions. Fluid Dyn. Res. 8, 85–100.

Smith, N.R., 1993. Ocean modeling in a global ocean observing system. Rev. Geophys. 31 (3), 281–317.

Stigebrandt, A., 1985. A model for the seasonal pycnocline in rotating systems with application to the Baltic proper. J. Phys. Oceanogr. 13, 1392–1404.

Thacker, W.C., Lewandowicz, R., 1996. Climatic indices, principal components and the Gauss–Markov theorem. J. Clim. 9 (8), 1942–1958.

Trask, R.P., Briscoe, M.G., 1983. Detection of Massachusetts Bay internal waves by the synthetic aperture radar (SAR) on SEASAT. J. Geophys. Res. 88 (C3), 1789–1799.

Tucker, J., Sheats, N., Giblin, A.E., Hopkinson, C.S., Montoya, J.P., 1999. Using stable isotopes to trace sewage-derived material through Boston Harbor and Mass. Bay. Mar. Environ. Res. 48, 353–375.

Turner, J.T., 1992. Planktonic copepods of Boston Harbor, Massachusetts Bay and Cape Cod Bay. Hydrobiologia 293, 405–413.

von Storch, H., Frankignoul, C., 1998. Empirical modal decomposition in coastal oceanography. In: Brink, K.H., Robinson, A.R. (Eds.), The Sea: The Global Coastal Ocean I, Processes and Methods, vol. 10, Wiley, New York, NY.

Verlaan, M., Heemink, A.W., 1997. Tidal flow forecasting using reduced rank square root filters. Stochastic Hydrol. Hydraul. 11 (5), 349–368.

Voorrips, A.C., Heemink, A.W., Komen, G.J., 1999. Wave data assimilation with the Kalman filter. J. Mar. Syst. 19 (4), 267–291.

Wallace, G.T., Braasch, E.F. (Eds.), 1996. Proceedings of the Gulf of Maine Ecosystem Dynamics: A Scientific Symposium and Workshop. The Regional Association for Research on the Gulf of Maine, RARGOM report 97-1.

Woodcock, A.F., 1984. Winds, upwelling and fog at Cape Cod Canal, Massachusetts. J. Clim. Appl. Meteorol. 23, 611–616.

Wunsch, C., 1996. The Ocean Circulation Inverse Problem. Cambridge Univ. Press.